Department of Micro- and Nanosciences

Novel light sources and high-resolution interferometric applications

Igor Shavrin

Aalto University

DOCTORAL DISSERTATIONS

Aalto University publication series
DOCTORAL DISSERTATIONS 204/2013

Novel light sources and high-resolution interferometric applications

Igor Shavrin

A doctoral dissertation completed for the degree of Doctor of Science (Technology) (Doctor of Philosophy) to be defended, with the permission of the Aalto University School of Electrical Engineering, at a public examination held at the lecture hall TU1 of the TUAS building (Otaniementie 17, Espoo, Finland) on the 9th of December 2013 at 13.

Aalto University
School of Electrical Engineering
Department of Micro- and Nanosciences
Fiber Optics Group

Supervising professor
Prof. Markku Sopanen

Thesis advisor
Dr. Hanne Ludvigsen

Preliminary examiners
Prof. Tim Birks, University of Bath, UK
Prof. Alexei Kamshilin, University of Eastern Finland, Finland

Opponent
Prof. Ole Bang, Technical University of Denmark, Denmark

Aalto University publication series
DOCTORAL DISSERTATIONS 204/2013

ISBN 978-952-60-5472-8
ISBN 978-952-60-5473-5 (pdf)
ISSN-L 1799-4934
ISSN 1799-4934 (printed)
ISSN 1799-4942 (pdf)
http://urn.fi/URN:ISBN:978-952-60-5473-5

Unigrafia Oy
Helsinki 2013

Finland

441 697
Printed matter

Author
Igor Shavrin

Name of the doctoral dissertation
Novel light sources and high-resolution interferometric applications

Publisher School of Electrical Engineering

Unit Department of Micro- and Nanosciences

Series Aalto University publication series DOCTORAL DISSERTATIONS 204/2013

Field of research Photonics

Manuscript submitted 9 September 2013 **Date of the defence** 9 December 2013

Permission to publish granted (date) 14 November 2013 **Language** English

☐ **Monograph** ☒ **Article dissertation (summary + original articles)**

Abstract

This thesis focuses on selected fundamental aspects of fiber-based supercontinuum light sources and presents two case studies of high-resolution optical interferometry.

Most commonly, supercontinuum light is generated by pulsed laser sources, so that strong intensity fluctuations are inherent in the emitted light. For applications, which require broadband continuous-wave illumination, a new concept of a broadband light source based on dispersive stretching of supercontinuum light pulses is presented. This concept was found to be able to provide intensity fluctuations below 1 % in the output light.

Supercontinuum generation in multimode fibers involves two major aspects that make it differ from continuum generation in single-mode fibers; much higher powers can be obtained without damaging the fiber and different spectral properties become accessible with the higher-order modes. To explore these possibilities, a numerical solver for simulation studies of supercontinuum generation in multimode fibers was developed. First, the solver was used to demonstrate the polarization dynamics of the supercontinuum generated by two degenerate fiber modes in a non-birefringent microstructured fiber. Next, the operation of the solver was verified by comparing the simulated and measured supercontinua produced in a suspended-core fiber. The influence of the higher-order modes became apparent already at lower pump powers.

As a case study of applications where broadband light sources are needed, an interferometer was developed to characterize surface vibrations in micro-mechanical resonators. The measurement principle was based on phase-shifting white-light interferometry (PS-WLI) with stroboscopic illumination. An analysis method was developed which made it possible to detect vibration amplitudes below 100 picometers. Further, it was found that for the best performance of PS-WLI an optimal spectral width of the illuminating light source is required, which in the presented setup was closely matched by a simple green light-emitting diode (LED). The pulse duration obtained from the LED allowed imaging out-of-plane vibration fields in a micro-mechanical plate resonator at frequencies up to 14 MHz, which is about 10 MHz higher than what has previously been reported. In principle, the achieved amplitude detection limit could allow even higher frequencies.

Additionally, a simple interferometric gas refractometer based on a hollow-core photonic band-gap fiber was developed and characterized. Using a tunable laser source, spectrally resolved measurements of both the refractive index and the absorption coefficient of gaseous analytes could be measured with high sensitivity. With this device, the refractive index of an air-acetylene mixture was measured with a resolution of $4 \cdot 10^{-7}$ RIU (refractive index units) in the spectral range from 1525 nm to 1545 nm.

Keywords supercontinuum generation, multimode fibers, white-light interferometry

ISBN (printed) 978-952-60-5472-8 **ISBN (pdf)** 978-952-60-5473-5

ISSN-L 1799-4934 **ISSN (printed)** 1799-4934 **ISSN (pdf)** 1799-4942

Location of publisher Helsinki **Location of printing** Helsinki **Year** 2013

Pages 116 **urn** http://urn.fi/URN:ISBN:978-952-60-5473-5

Aalto-yliopisto

Tiivistelmä

Aalto-yliopisto, PL 11000, 00076 Aalto www.aalto.fi

Tekijä
Igor Shavrin

Väitöskirjan nimi
Novel light sources and high-resolution interferometric applications

Julkaisija Sähkötekniikan korkeakoulu

Yksikkö Mikro- ja nanotekniikan laitos

Sarja Aalto University publication series DOCTORAL DISSERTATIONS 204/2013

Tutkimusala Fotoniikka

Käsikirjoituksen pvm 09.09.2013 **Väitöspäivä** 09.12.2013

Julkaisuluvan myöntämispäivä 14.11.2013 **Kieli** Englanti

☐ **Monografia** ☒ **Yhdistelmäväitöskirja (yhteenveto-osa + erillisartikkelit)**

Tiivistelmä

Väitöskirjassa on tutkittu spektriltään laajakaistaisen valon, ns. superkontinuumivalon, aikaansaamista optisissa kuiduissa sekä kahta korkean erotuskyvyn optista interferometriatekniikkaa.

Superkontinuumivalo tuotetaan yleensä syöttämällä optiseen kuituun lyhyitä suuritehoisia, yksivärisiä laserpulsseja, jotka vuorovaikuttaessaan kuidussa tuottavat epälineaaristen optisten prosessien kautta spektriltään laajakaistaista pulssitettua valoa. Usein tarvitaan kuitenkin ajassa jatkuvaa emissiota. Työssä kehitettiin menetelmä, jossa valopulsseja levitetään aika-avaruudessa dispersiota hyväksi käyttäen siten, että vierekkäiset pulssit levenevät toistensa päälle. Näin onnistuttiin luomaan superkontinuumivaloa, jonka intensiteetti vaihteli alle 1 %.

Voimakkaiden superkontinuumipulssien tuottamisessa monimuotokuidut ovat etusijalla yksimuotokuituihin verrattuna. Ne kestävät suurempia pulssitehoja ja korkeamman kertaluvun muodot mahdollistavat uudet spektriominaisuudet. Näiden mahdollisuuksien tutkimiseksi kehitettiin numeerinen laskumenetelmä, jolla superkontinuumin syntyä monimuotokuiduissa voidaan simuloida. Menetelmää sovellettiin ulostulopulssien polarisaatiodynamiikan selvittämiseen tapauksessa, jossa ei-kahtaistaittavassa monimuotoisessa mikrorakennekuidussa etenee kaksi degeneroitunutta muotoa. Simulaatiotuloksia verrattiin myös kokeellisiin mittauksiin tapauksessa, jossa käytettiin erityisen ohutytimistä mikrorakennekuitua. Korkeampien muotojen vaikutus kävi ilmeiseksi jo alhaisilla pumppaustehoilla.

Sovelluksena laajakaistaisen valon käytölle työssä kehitettiin mittaussignaalin vaiheinformaatiota hyödyntävä stroboskooppinen valkoisen valon interferometri, jolla voitiin tutkia mikromekaanisten resonaattorien värähtelyominaisuuksia. Analyysimenetelmää kehittämällä kyettiin havaitsemaan alle 100 pikometrin värähtelyamplitudeja. Parhaaseen suorituskykyyn pääsemiseksi valolähteen spektriltä vaaditaan tiettyä leveyttä, joka pystyttiin toteuttamaan yksinkertaisella LEDillä. Koejärjestelyllä kyettiin mittaamaan värähtelyjä aiemmin raportoitua korkeammilla taajuuksilla.

Lopuksi väitöskirjassa esitetään optiseen interferometriaan perustuva kaasun taitekertoimen mittausmenetelmä, jossa kaasu vuorovaikuttaa onttoytimisessä fotonikidekuidussa etenevän, aallonpituudeltaan viritettävän laservalon kanssa. Mittaustuloksena saadaan sekä kaasun absorption että sen taitekertoimen spektrit suurella herkkyydellä. Esimerkkinä onnistuttiin mittaamaan ilma-asetyleeniseoksen taitekerroin $4 \cdot 10^{-7}$ suuruisella erotuskyvyllä aallonpituusvälillä 1525 – 1545 nm.

Avainsanat superkontinuumivalo, monimuotokuitu, valkoisen valon interferometria

ISBN (painettu) 978-952-60-5472-8 **ISBN (pdf)** 978-952-60-5473-5

ISSN-L 1799-4934 **ISSN (painettu)** 1799-4934 **ISSN (pdf)** 1799-4942

Julkaisupaikka Helsinki **Painopaikka** Helsinki **Vuosi** 2013

Sivumäärä 116 **urn** http://urn.fi/URN:ISBN:978-952-60-5473-5

Preface

The research work summarized in this thesis has been carried out in the Fiber Optics group at the Department of Micro and Nanosciences of Aalto University (formerly Helsinki University of Technology) during the years 2009-2013. I would like to express my deepest gratitude to my supervisor Docent Hanne Ludvigsen for the opportunity to work in her research group and for her supervision, support and encouragement throughout the course of this work. I also highly appreciate being given the possibility to gain experience in various fields of optics.

I am most grateful to my thesis advisor Dr. Steffen Novotny with whom I have had the privilege to work with closely. I am also very thankful to Steffen for his guidance, support and friendship and for many days in the lab we have spent together.

I am very thankful to Kimmo Kokkonen for his advice and motivation during the development of white-light interferometer, Lauri Lipiäinen for performing the vibration measurements and Roman Khakimov for his help and long discussions on various subjects. I am very thankful to Docent Andriy Shevchenko for his enthusiasm and guidance during our long days in the lab at the beginning of this work. I am very thankful to Professor Matti Kaivola and all the co-authors for their important contribution to this work.

I also thank Vasuki Durairaj for her help, long discussions and very nice cakes which made our worktime sweeter. I thank Aleksandr Kravchenko for his help in the cleanroom and for introducing me to exciting activities like flying remote controlled aircraft models and scuba diving which opened up a different view of the Finnish skies and waters for me. I also thank Mikhail Erdmanis, Peter Tvarožek and Alexander Savelyev for their help and the good times we have shared.

I thank all my friends for the wonderful and relaxing moments we have shared during the years.

The funding of this work has been provided by the Graduate School on Modern Optics and Photonics and the Academy of Finland as part of the Research Programme on “Photonics and Modern Imaging Techniques” (project 134857) and project 136351.

Finally, I heartily thank my parents Sergiy and Nina Shavrin for their continuous support, their love and countless hours on Skype which brought home a little closer. Also, I thank my brother Sergiy and his wife Vira for their support and entertaining and enjoyable discussions.

Espoo, September 9, 2013,

Igor Shavrin

Contents

List of Publications

This thesis consists of an overview and of the following publications which are referred to in the text by their Roman numerals.

I I. Shavrin, S. Novotny, A. G. Savelyev, S. C. Buchter, and H. Ludvigsen. Simple visible supercontinuum light source with true continuous–wave output power. *Appl. Phys. Lett.*, **101**, 091112, August 2012.

II R. Khakimov, I. Shavrin, S. Novotny, M. Kaivola, and H. Ludvigsen. Numerical solver for supercontinuum generation in multimode optical fibers. *Opt. Express*, **21**, 14388, June 2013.

III I. Shavrin, S. Novotny, and H. Ludvigsen. Mode excitation and supercontinuum generation in a few–mode suspended–core fiber. *Submitted to Opt. Express*, 2013.

IV I. Shavrin, L. Lipiäinen, K. Kokkonen, S. Novotny, M. Kaivola, and H. Ludvigsen. Stroboscopic white-light interferometry of vibrating microstructures. *Opt. Express*, **21**, 16901, July 2013.

V I. Shavrin, S. Novotny, A. Shevchenko, and H. Ludvigsen. Gas refractometry using a hollow–core photonic bandgap fiber in a Mach–Zehnder–type interferometer. *Appl. Phys. Lett.*, **100**, 051106, January 2012.

Author's Contribution

The scientific results presented in this work have been carried out during the years 2009–2013. All publications are results of teamwork. Part of the results have been also presented by the author in international conferences.

Publication I: "Simple visible supercontinuum light source with true continuous–wave output power"

The author carried out the experiments, performed the calculations and contributed to the preparation of the manuscript.

Publication II: "Numerical solver for supercontinuum generation in multimode optical fibers"

The author performed the simulations and the polarization analysis, participated in the development of the numerical solver and contributed to the preparation of the manuscript.

Publication III: "Mode excitation and supercontinuum generation in a few–mode suspended–core fiber"

The author carried out the experiments, performed the simulations and contributed to the preparation of the manuscript.

Publication IV: "Stroboscopic white-light interferometry of vibrating microstructures"

The author developed the analysis program, analyzed the measurement results, contributed to the development of the code to control the experiment

and prepared the first draft of the manuscript.

Publication V: "Gas refractometry using a hollow–core photonic bandgap fiber in a Mach–Zehnder–type interferometer"

The author constructed the experimental setup, carried out the experiments, participated actively in the analysis of the results and in the writing of the manuscript.

Other peer–reviewed publications to which the author has contributed:

I. Shavrin, P. Tvarožek, M. Koyš, K. Schuster, S. Novotny, and H. Ludvigsen, "Extremely white supercontinuum generation in three–hole suspended–core fiber", in "CLEO/Europe and EQEC 2011 Conference Digest," (Optical Society of America, 2011), p. CF_P16.

List of abbreviations

ANDi	all-normal dispersion
CCD	charge-coupled device
FDA	frequency domain analysis
FEM	finite-element method
FT	Fourier transform
FWM	four-wave mixing
GNLSE	generalized nonlinear Schrödinger equation
GVD	group velocity dispersion
HC-PBF	hollow-core photonic bandgap fiber
HOM	higher-order mode
LED	light-emitting diode
MDW	minimum dispersion wavelength
MEMS	microelectromechanical system
MM-GNLSE	multimode generalized nonlinear Schrödinger equation
MOF	microstructured optical fiber
ODE	ordinary differential equation
OPLD	optical path length difference
PBF	photonic bandgap fiber
PCF	photonic crystal fiber
PSD	power spectral density

RIN	relative intensity noise
RIU	refractive index units
SCF	suspended-core fiber
SCG	supercontinuum generation
SEM	scanning electron microscopy
SMF	single-mode fiber
SPM	self-phase modulation
SRS	stimulated Raman scattering
SSFM	split-step Fourier method
TIR	total internal reflection
WLI	white-light interferometry
XPM	cross-phase modulation
ZDW	zero-dispersion wavelength

List of symbols

β	propagation constant $[1/m]$
β_2	group-velocity dispersion $[s^2/m]$
λ	free-space wavelength $[m]$
ω	angular frequency $[rad/s]$
c_0	the speed of light $[m/s]$
D	group-velocity dispersion coefficient $[ps/(km \cdot nm)]$
$\mathcal{F}$	Fourier transform operator
I	intensity $[W/m^2]$
k	wavenumber $[rad/m]$
n	refractive index
n_2	nonlinear index $[m^2/W]$

1. Introduction

During the past decade, following the first demonstration of supercontinuum generation in photonic crystal fibers in the beginning of 2000 [1], a completely new class of light sources with spectacular properties has emerged [2]. The sources are able to emit broadband light that can span in spectral frequency more than two octaves. Due to their extremely high brightness and excellent beam quality that allows for tight focusing, these fiber-based supercontinuum sources are also referred to as white-light lasers [3]. Pertaining to these remarkable properties, supercontinuum sources have become very popular in a wide range of applications, such as high-resolution optical frequency metrology [4, 5] and spectroscopy [6, 7], as well as in various sensing and imaging techniques [8–10].

Supercontinuum generation refers to a set of nonlinear optical processes taking place in a dielectric medium when an initially single-wavelength laser pulse is efficiently converted into new wavelengths while propagating in the medium. Typically, the dielectric medium is composed of a photonic crystal or microstructured optical fiber, which possesses a tiny core surrounded by a set of holes running through the length of the fiber [11, 12]. Supercontinuum sources owe their exceptional spectral properties particularly to the flexibility in the dispersion design offered by those fibers, as the spectral broadening of the laser pulses sensitively depends on the wavelength of the launched pulses relative to the dispersion profile of the fiber [13, 14].

The proper dispersion control has been the key to successfully shift the short wavelength edge of the continuum further into the ultraviolet, which has been one of the main aims in the recent supercontinuum source development [15]. However, fiber design approaches the limit for what can be reached using the fundamental fiber mode. This fact has turned the interest towards the use of higher-order modes in extending the range of supercontinuum radiation to even shorter wavelengths utilizing their unique dispersion properties [16, 17].

The present understanding of the processes involved in supercontinuum generation would not have been reached without detailed comparisons between experiments and numerical simulations. As a result, one can meanwhile observe for selected cases, such as the single-mode pulse propagation in silica fibers, a good agreement between experiments and numerical results. Extension of the theoretical framework to include higher-order modes in pulse propagation [18,19] has, certainly added to the complexity, but with enormous potential also to various other applications [20,21].

For the design of tailored broadband light sources it is equally important to reach not only a detailed understanding of the underlying complex dynamics of supercontinuum generation but also to identify the requirements set to the light source from the application point of view.

Among the wide range of applications of supercontinuum light, low-coherence interferometry is one that will particularly benefit from the high brightness and favorable spectral properties of supercontinuum light. The broad spectrum translates to a short coherence length, which helps improve the resolution of such techniques as optical-coherence tomography [22] and white-light interferometry [23].

The thesis is divided in two parts: First, the fundamentals of various types of microstructured optical fibers (Ch. 2) and basic aspects of supercontinuum generation in them are considered in Sec. 3.1. Then, practical means to convert a pulsed supercontinuum source to provide quasi-continuous-wave radiation is described in Sec. 3.2 [Publication I]. Section 3.3 presents a numerical solver developed for simulating supercontinuum generation in multimode fibers. The solver is applied to study the influence of higher-order modes on supercontinuum generation in a non-birefringent multimode fiber and in a suspended-core fiber [Publication II and Publication III].

The second part of the thesis focuses on the two examples of high-resolution optical interferometry. Section 4.2 describes the design of a white-light interferometer with stroboscopic illumination and introduces the special data analysis method that was developed. The performance of the interferometer is demonstrated by mapping surface vibration fields for a selection of out-of-plane vibration modes of a square-plate silicon MEMS resonator [Publication IV]. Section 4.3 describes a fiber-based Mach-Zehnder-type interferometer that was designed and used for simultaneous measurements of both the refractive index and the absorption coefficient of gas samples infiltrated into a hollow-core photonic band-gap fiber. In this particular case, the measurement was performed for acetylene [Publication V].

2. Optical fibers

Light guidance was demonstrated in a water stream as early as 1840 but this technique was of limited use for the transmission of light, except for laboratory demonstration purposes on optics. With the invention of glass optical fibers in the early 20th century, more practical light guidance became possible. This lead to many applications, for instance imaging of remote locations by using a bunch of thin glass fibers, however, light transmission over long distances was not yet possible at that time due to the high losses. In 1966 it was estimated that the minimum fundamental limit for losses in glass fibers had not been reached yet [24]. According to these predictions, improvement of the glass purity could reduce the attenuation in fibers below 20 dB/km, an important milestone towards practical long-distance fiber-optic communication systems. Over the last five decades, evolution of fiber fabrication and design technologies have enabled to achieve attenuation levels as low as 0.2 dB/km [25] and provided a control of other light guidance properties. Information transmission became possible over very long distances and has led to additional application areas for optical fibers beyond the telecommunication industry [26], extending to fields such as sensing, medical imaging and many more.

The schematic of a simple optical fiber is shown in Fig. 2.1. This fiber consists of two concentric glass layers, namely the core and the cladding. In addition, the fibers are usually coated with a hard polymer layer that shields the glass layers from abrasion, moisture and improves the mechanical strength [27–29].

In conventional optical fibers, like the one shown in Fig. 2.1, light guidance is achieved by total internal reflection (TIR) at the core-cladding interface. According to the Snell-Descartes law, TIR requires that the refractive index of the core is higher than that of the cladding, see the plot in Fig. 2.1. Usually, the index contrast between the core and cladding is created by adding dopants into either the core or the cladding during fiber manufacturing.

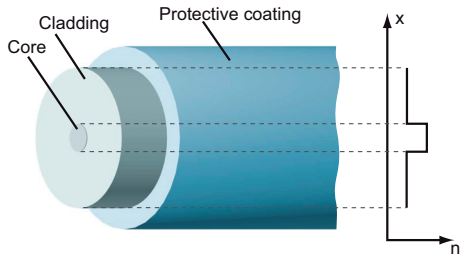

Figure 2.1. Schematic representation of a simple step-index optical fiber together with the refractive index profile.

Conventional fibers are well known as a key component in modern telecommunication systems, however their use in other areas of research and industry is quite limited. After achieving nearly the minimum fundamental limit for losses, the interest of the research community in optical fibers started to decline. This changed, however, with the demonstration of a completely new optical fiber concept.

In 1991, Philip Russell suggested in unpublished work a fiber, which employs the unique properties of photonic crystals for light guidance [11,30,31]. It was predicted that such photonic crystal fibers (PCFs) could, in principle, enable light guidance even in a hollow core. However, the manufacturing of PCFs was very challenging and the first operational PCF had a solid core and was guiding the light similarly to conventional fibers. Interestingly, the fiber was found to support only the fundamental mode over a very broad spectral range spanning from mid-infrared to the blue [30]. A few years later, light guidance in an air hole was finally demonstrated [32]. From this point on, the PCFs have revolutionized optical fiber technology and broadened the scope of fiber-optic applications thanks to the unprecedented flexibility in the design of their optical properties [11,31,33–39].

Photonic crystal fibers, in which light guidance is achieved due to an effective index contrast, are called microstructured optical fibers (MOFs). In contrast to conventional fibers, MOFs are typically made of a single material with the cladding formed by a matrix of micron-sized air-holes running along the fiber length. The microstructure provides lower average refractive index of the cladding compared to the solid core, hence light guidance is achieved by the so called modified TIR. The schematic view of a typical MOF, together with it's refractive index profile, is shown in Fig. 2.2(a). In MOFs, the modulation of the refractive index not only creates an effective index contrast but also strongly affects the waveguiding properties due to the significant dependence of the average refractive index on the wavelength. As a result of

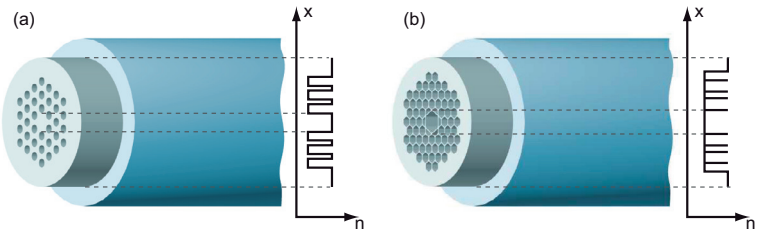

Figure 2.2. Schematic view of an index guiding MOF (a) and a HC-PBF (b) together with their refractive index profiles.

this unique wavelength dependence, the first demonstrated PCF was found to be endlessly single-mode [30, 40]. Equally important, the PCF technology also enables single-mode guidance in a MOF with a very large core [41]. Such large-mode area MOFs are capable of high-power light delivery with negligible nonlinearities and excellent beam quality.

On the other hand, by increasing the air filling ratio in MOFs, the core size can be significantly reduced, resulting in extreme light confinement, which effectively boosts nonlinearities. The increase of non-linear effects in MOFs can be used to efficiently generate supercontinua, which has lead to the development of novel light sources with extremely broadband spectra and brightness comparable to that of lasers [1, 42, 43].

A conceptually different light guidance mechanism is utilized in another kind of PCFs, called photonic bandgap fibers (PBFs) [44, 45]. In these fibers, the low-index core is surrounded by a microstructure with a higher average refractive index, which makes TIR impossible. The light guidance, however, is achieved exclusively due to photonic band-gap effect, giving the name of these fibers. The photonic bandgap effect also allows for light guidance in a hollow core surrounded by a properly engineered microstructure [32], as illustrated in Fig. 2.2(b).

Since the introduction of hollow-core PBFs (HC-PBFs), their potential for sensor applications was recognized. The core can be easily infiltrated with an analyte providing an excellent overlap with the guided light. Even with a small sampling volume a high sensitivity can be achieved [38, 39, 46–48]. Since then, various sensor designs were proposed, which allow monitoring the refractive index [49, 50] of gaseous analytes, gas sensing [46, 51–54], as well as measuring the strain [55, 56] and temperature [56, 57]. For instance, in Publication V, we demonstrated how the HC-PBF can be used for high-resolution spectrally-resolved measurements of the complex refractive index of gases.

Modes and dispersion. Numerous characteristics are needed to describe the light propagation in optical fibers. While the detailed description of these characteristics can be found from a wide range of textbooks [33, 34, 58, 59], in this section I shall only briefly introduce the most important characteristics essential for the other parts of the thesis.

Propagation of light in optical fibers is most conveniently described in terms of the guided modes. Guided modes are the solutions of Maxwell's equations for the boundary conditions defined by the fiber cross-section. All fiber modes have a distinct propagation constant and a characteristic transverse field distribution which remains constant during propagation.

According to the modal description, the complex amplitude of the monochromatic electromagnetic field $U(x, y, z, \omega)$ propagating along the fiber with N guided modes can be represented as a sum of mode-fields

$$U(x, y, z, \omega) = \sum_{m=1}^{N} U_m(x, y, z, \omega), \tag{2.1}$$

where ω is the angular frequency and x, y, z are the spatial coordinates.

Furthermore, translational invariance of the optical fibers allows separating the modal fields into transverse $F_m(x, y, \omega)$ and longitudinal $A_m(z, \omega)$ components

$$U_m(x, y, z, \omega) = F_m(x, y, \omega) \cdot A_m(z, \omega) \cdot e^{i\beta_m(\omega)z}, \tag{2.2}$$

where $\beta_m(\omega)$ is the real valued propagation constant of m-th mode, which is equivalent to the phase change per unit of length. This separation significantly simplifies the modeling of light propagation in fibers, since the only variable remaining is the amplitude, while the propagation constants and the transverse field distributions of the guided modes depend only on the fiber characteristics.

The number of guided modes can be controlled through the design of fiber geometry. It is possible to create optical fibers, which support only the fundamental guided mode at least within a certain spectral range, as illustrated in Fig 2.3. For instance, in conventional fibers this is usually achieved by reducing core diameter to $\sim 8\,\mu$m with a core-cladding index contrast of $\sim 10^{-3}$ RIU (refractive index units). In comparison, the design of the microstructured region in MOFs, provides more flexible control of the number of guided modes [60].

It is important to note that for certain symmetries, a fiber may have modes with equal propagation constants, which are called degenerate [61–63]. For instance, the conventional non-birefringent fibers with circular core have two degenerate fundamental modes which differ only by the state of polarization.

The propagation constant of a fiber mode is a function of frequency and is therefore responsible for chromatic dispersion. In optical fibers, total chro-

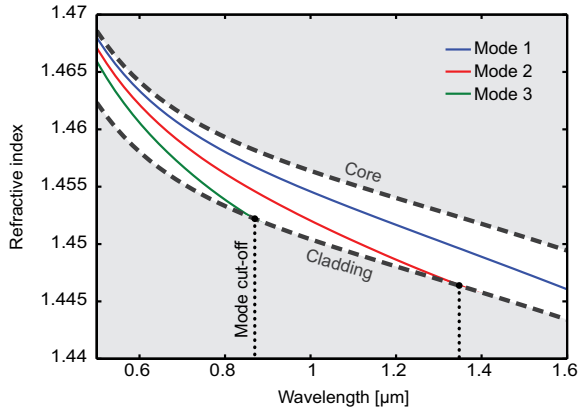

Figure 2.3. Effective indices of a few selected modes in a conventional optical fiber (solid lines) together with the refractive indices of the core and the cladding (thick dashed lines). The mode cut-off wavelengths (dotted lines) of modes 2 and 3 are indicated.

matic dispersion depends on both the dispersive properties of fiber material and the waveguide dispersion determined by the fiber geometry. In analogy to the refractive index of a homogenous medium, one can introduce the effective refractive index of a fiber mode as

$$n_{eff}(\omega) = \frac{c_0 \cdot \beta(\omega)}{\omega}, \tag{2.3}$$

where c_0 is the speed of light. Effective refractive indices of a guided modes are always located in between the refractive indices of the core and of the cladding, as illustrated in Fig 2.3. When the effective index of a mode becomes equal to the cladding index, the mode is no longer guided at longer wavelengths, as indicated in Fig. 2.3. This wavelength is also referred to as mode cut-off. In conventional fibers, only the fundamental mode has no cut-off wavelength.

The effects of dispersion on guided light are best illustrated by expanding the propagation constant in the vicinity of a conveniently chosen frequency ω_0 using Taylor expansion

$$\beta(\omega) = \beta_0 + \beta_1(\omega - \omega_0) + \frac{\beta_2}{2}(\omega - \omega_0)^2 + \dots, \text{ where } \beta_n = \left.\frac{\partial^n \beta}{\partial \omega^n}\right|_{\omega=\omega_0}. \tag{2.4}$$

This enables to obtain the two most important parameters β_1 and β_2, which describe the group velocity ($v_g = 1/\beta_1$) and the group velocity dispersion (GVD) β_2, i.e. the velocity at which the pulse envelope moves and its temporal broadening, respectively. These two parameters are very important for the understanding and characterization of dispersion and are typically sufficient for the description of narrow-band light propagation. The propagation of broadband light in fibers, however, requires the knowledge of the complete functional dependence of $\beta(\omega)$.

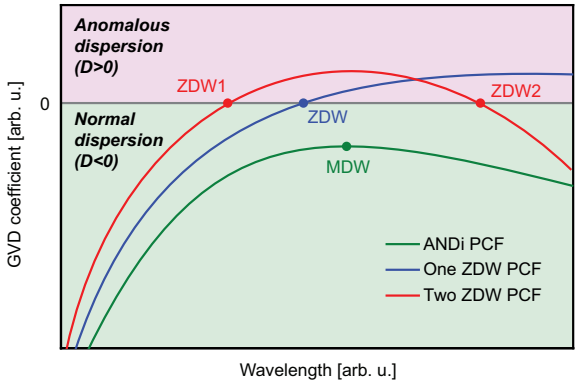

Figure 2.4. Different group-velocity dispersion profiles are compared, featuring two (red line), one (blue line) ZDWs or are located completely within the normal dispersion regime with a MDW (green line).

For practical purpose, the GVD is often presented in terms of the GVD coefficient D, which is the rate of pulse broadening per unit of length per unit of spectral width. It is related to β_2 as

$$D = -\frac{2\pi c_0}{\lambda^2}\beta_2 \simeq -\frac{\lambda}{c_0}\frac{\partial n_{eff}^2}{\partial \lambda^2}, \tag{2.5}$$

where λ is the free-space wavelength.

The dispersion curve is typically divided into the two distinct parts, the normal and anomalous regime. Dispersion is called normal when $\beta_2 > 0$ ($D < 0$) and it is anomalous when $\beta_2 < 0$ ($D > 0$). Special attention is paid to the wavelength, where the GVD equals to zero, which is called zero-dispersion wavelength (ZDW). Ideally, a narrow-band light pulse with a central wavelength that is equal to ZDW, is expected to propagate over long distances without broadening, though it is rarely observed in practice due to the presence of higher order dispersion.

The location of the ZDW is defined by the fiber material but can also be modified by altering the fiber geometry. The highest flexibility in tailoring the dispersion properties are offered by MOFs [64]. For certain designs the fiber may exhibit two ZDW points or none of them, as illustrated in Fig. 2.4 by the red or green curve, respectively. Fibers with only normal dispersion are called all-normal dispersion (ANDi) fibers [65]. Analogously to the definition of the ZDW, the minimum dispersion wavelength (MDW) is often defined as a parameter of ANDi fibers, where the dispersion is closest to zero.

The possibility to tailor the dispersion properties is important for nonlinear applications, in particular for supercontinuum generation, as will be discussed in the next chapter.

Calculation of fiber modes and dispersion. Mode fields and the corresponding propagation constants can be obtained by solving Maxwell's equations for a fiber cross-section either analytically or numerically. However, analytical solutions can be obtained only in a few specific cases for a simple fiber geometry, while more complex geometries require the use of numerical methods. One of the most popular numerical approaches is the finite-element method (FEM), which allows for solving Maxwell's equations for arbitrary geometries and thus is well suitable for the mode analysis of PCFs. Commercially available FEM solvers are routinely used for modeling of light propagation in optical fibers.

In this thesis, all modal and dispersion calculations were performed using the eigenmode FEM solver provided in the COMSOL Multiphysics® package [66]. This software package solves the full-vectorial Maxwell's equations providing accurate mode-fields and the propagation constants, including the polarization properties of the analyzed fiber geometry.

3. Supercontinuum light sources

Light sources based on supercontinuum generation in optical fibers become increasingly popular in various areas of science and industry. They emit extremely broadband light with high brightness and beam quality, which are comparable to those of lasers. The unique properties of supercontinuum sources have already found applications in numerous fields, including optical frequency metrology [43, 67], optical communications [68], spectroscopy [6] and many others. For instance, the small coherence length of the emitted broadband light can be utilized to improve performance of low-coherence interferometry techniques, such as optical-coherence tomography [69] and scanning white-light interferometry [9].

In this chapter, the basics of supercontinuum generation are introduced, before the principle of a continuous-wave supercontinuum light source [Publication I] is described. Finally, the numerical and experimental studies of supercontinuum generation in multimode fibers are presented [Publication II and Publication III].

3.1 Basics of supercontinuum generation

Any dielectric medium has a nonlinear response when high-intensity light is propagating through it. The interplay between various nonlinear effects results in the generation of new frequencies, broadening the input light to a spectral continuum at the output. This process is known as supercontinuum generation (SCG).

In the 1960s, spectral broadening of high intensity pulses was first demonstrated in liquids [70, 71] and then in bulk crystals and glasses [72, 73]. These experiments have shown that efficient spectral broadening requires a long interaction path and enormous power levels. The idea of developing novel light source based on this principle was very promising but required huge and ex-

pensive high power lasers. However, extreme intensities can lead to the self-focusing effect resulting in beam filamentation and possible damage of the nonlinear material.

Few years later, optical fibers were demonstrated to be good candidates for efficient excitation of nonlinearities due to the long interaction path and strong light confinement in the core [74–77]. This allowed for significant reduction of required laser power to only a few kilowatts [78], instead of more than 100 megawatts for bulk materials [72]. Moreover, supercontinua generated in a single-mode fiber showed a high beam quality.

Another important advantage of using optical fibers for SCG is the ability to tailor their dispersion properties. As will be discussed in more details later in this section, dispersion plays a very important role in SCG, as it defines the dynamics of nonlinear processes and the overall efficiency of spectral broadening. Early experiments have shown that the highest spectral broadening can be achieved when the wavelength of laser pulse is located in the vicinity of ZDW. Optical fiber technology provides a control over the position of ZDW thanks to the waveguide contribution to the effective refractive index of a fiber mode. However, with conventional fiber technology it was not possible to realize a ZDW below that of the fiber material ($\approx$ 1280 nm for fused silica), where most lasers are operated.

Soon after their first introduction, MOFs became particularly favored for generating supercontinua due to their unprecedented flexibility in the design of the dispersion characteristics and the extreme light confinement. With MOFs, it became possible to realize a ZDW in the visible spectral range and thus enable the generation of a visible supercontinuum in optical fibers [1]. The unprecedented flexibility in the dispersion control allowed for matching of ZDW to the operation wavelength of available high power lasers, which together with the achievable high nonlinearity, have boosted the interest in theoretical and experimental research of SCG.

A supercontinuum in the visible spectral range has also been generated in tapered conventional germanosilicate fibers [79]. This alternative approach makes use of readily available and inexpensive telecommunications fibers. This way, good coupling to other fiber components is provided. However, tapered fibers require special protection of the tapered region from both mechanical damage and dust, as light scattering can otherwise easily affect the performance of light guidance. In practice, this is difficult to achieve since strong light confinement in the tapered region requires very low refractive index of the surrounding medium, and thus cannot be covered with a hard protective

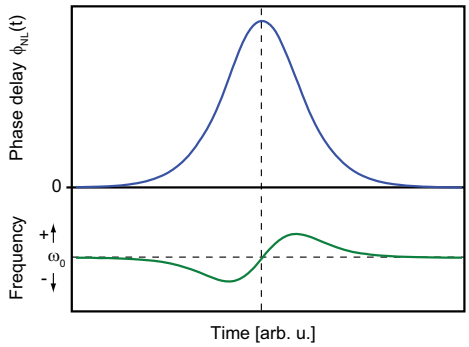

Figure 3.1. SPM results in a frequency shift due to time-dependent phase delay caused by the intensity variation in a light pulse.

coating. For this reason, MOFs have more commonly been used for SCG.

The dynamics of the nonlinear processes involved in SCG are very complex, which sometimes makes it difficult to isolate the contribution of different mechanisms. Nevertheless, it is useful to study these mechanisms first independently in order to gain a fundamental understanding of the underlying physical processes.

3.1.1 Nonlinear Kerr effect

The temporal variation of intensity in a pulse $I(t)$ causes the proportional variation of the local refractive index in a medium $\Delta n(t) = n_2 I(t)$, which is called nonlinear Kerr effect. There are three major effects arising from Kerr nonlinearity: self-phase modulation (SPM), cross-phase modulation (XPM) and four-wave mixing (FWM).

Self and cross-phase modulation result in a time-dependent phase delay either in the same pulse ($\phi_{NL} = k_0 \cdot n_2 \cdot I \cdot z$) or in a co-propagating pulse ($\phi_{NL} = k_0 \cdot n_2 \cdot (I_1 + 2I_2) \cdot z$), respectively. A time-dependent phase delay implies a frequency shift with magnitude $\delta\omega(t) \equiv -d\phi_{NL}/dt$ and therefore leads to nonlinear chirping of optical pulses and the generation of new frequency components, as illustrated in Fig. 3.1.

Four wave mixing is a parametric process which results in the generation of new frequencies. It involves two pump waves with frequencies ω_1 and ω_2 and two new waves generated at frequencies ω_3 and ω_4. In single-mode optical fibers, however, it is often assumed that the two pump waves have equal frequencies ($\omega_1 = \omega_2$), so that the FWM is degenerate.

According to energy conservation, the frequencies must satisfy the following condition

$$\omega_3 + \omega_4 = \omega_1 + \omega_2. \tag{3.1}$$

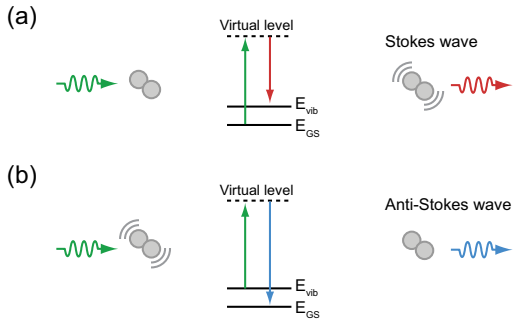

Figure 3.2. Generation of (a) Stokes and (b) anti-Stokes waves in stimulated Raman scattering process.

In addition, momentum conservation between the four interacting photons requires the phase mismatch Δk to be equal to zero

$$\Delta k = k_3 + k_4 - k_1 - k_2 = 0, \tag{3.2}$$

where $k_j = n(\omega_j) \cdot \omega_j / c_0$ [80]. At wavelengths near the ZDW, the phase mismatch (Δk) is minimized [81, 82], which thus results in a significant contribution of FWM to the generated supercontinuum [83–85].

3.1.2 Stimulated Raman Scattering

Raman scattering is an inelastic scattering process in which photons exchange energy with optical phonons. This process can be explained with the help of virtual energy levels introduced into the energy diagram, as shown in Fig. 3.2. During interaction an incident photon may transfer part of its energy and excite an optical phonon with energy E_{vib}. As a result, the photon becomes red-shifted. In case, an incident photon interacts with an already existing phonon, the photon may acquire energy and become blue-shifted. Therefore, Raman scattering results in appearance of two additional spectral components placed symmetrically around the pump with a frequency shift depending on the vibration energy levels of the medium ($\Delta\nu_R \sim 13$ THz for fused silica fibers). The red-shifted light, often called Stokes wave, is usually much stronger than the blue-shifted anti-Stokes wave due to the fact that higher vibration levels are less populated than the ground-state level. Generally, Raman scattering is a relatively weak effect. However, if the medium can force scattered photons to remain within it, they will stimulate the emission of new red or blue shifted photons, greatly amplifying the Stokes and anti-Stokes components. This process is called stimulated Raman scattering (SRS) and plays an important role in SCG.

Stimulated Raman scattering is one of the primary nonlinear effects in SCG

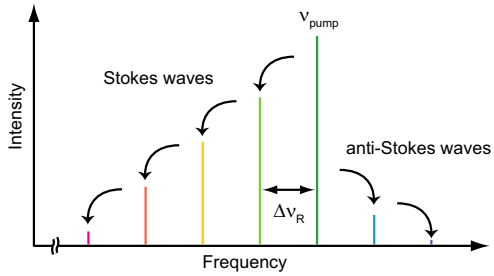

Figure 3.3. Cascaded SRS results in generation of secondary spectral components at intervals $\Delta\nu_R$.

with long pump pulse durations ranging from picoseconds up to continuous-wave pumping, and it is the dominant effect when pumped in the normal dispersion regime.

Under high pump powers, when even the power of the Stokes wave exceeds the Raman threshold, the Raman effect can repeat to produce a secondary Stokes wave [86]. This process is called cascaded SRS and may repeat several times during propagation generating multiple equidistant spectral components, as illustrated in Fig. 3.3. If a phase matching condition holds for the SRS generated frequencies, FWM may contribute significantly and result in a very smooth continuum extending to the blue [83].

3.1.3 Influence of dispersion

Since dispersion is a linear effect, it does not result in generation of new frequencies, however, it has a strong impact on the character of nonlinear interactions.

In case pumping takes place in the normal dispersion regime ($D < 0$), the resulting supercontinuum is mainly determined by SPM and SRS. The pump pulse undergoes simultaneous broadening in both frequency and time domains, which results in a spectrum with relatively narrow bandwidth but high stability.

If the dispersion regime at pump wavelength is anomalous ($D > 0$), a nonlinear chirp due to SPM and a linear chirp caused by the dispersion may counteract and result in the formation of solitons. At sufficiently high power, the input pump pulse will form a higher-order soliton which eventually brakes into fundamental solitons. During the decay, every fundamental soliton emits a blue-shifted non-solitonic radiation at wavelength which depends on the phase-matching condition with the soliton itself, as illustrated in Fig. 3.4. This process provides the initial spectral broadening and results in formation

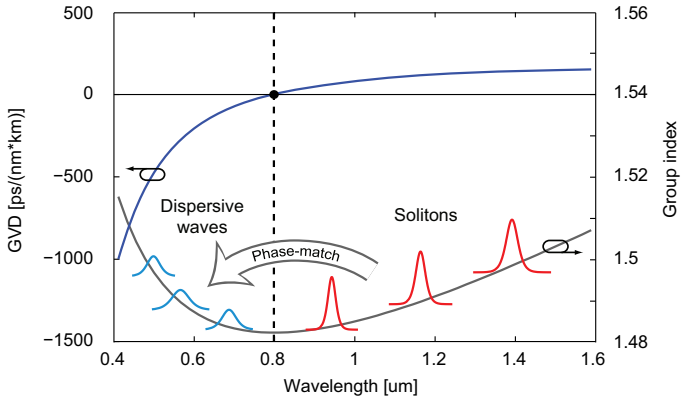

Figure 3.4. Illustration of soliton dynamics and generation of dispersive waves when pumping takes place in the anomalous dispersion regime. The dispersive waves are non-solitonic pulses which appear in the normal dispersion range at phase matched wavelengths with the corresponding solitons.

of the spectrum with a gap around the ZDW [87]. After this mechanism, a complex interaction among FWM, SRS, and dispersion fills the gap and the spectrum develops into a flat continuum [87, 88]

3.2 Supercontinuum source with continuous-wave output

Most commonly, supercontinua are generated from short, high-intensity laser pulses ranging from the femtosecond to nanosecond regime. Also, cw-lasers with high average powers have been used providing high spectral power densities and smooth spectra. Independent of the pump laser source employed, the generated supercontinuum light is temporally not constant, but is rather in a form of confined, high peak-power pulses or soliton-like structures [89, 90].

In Publication I, the concept of a simple fiber-based supercontinuum light source with a potential to emit light with a temporally stable power and tailored spectrum was studied both experimentally and computationally. The light source is based on the idea of dispersive time-stretching in an optical fiber to convert efficiently and in a completely passive way the high intensity supercontinuum pulses into a temporally constant output.

The proposed source consists of two main parts: a pulsed supercontinuum source and a conventional optical fiber as a dispersive medium for temporal pulse stretching, as illustrated in Fig. 3.5.

When broadband pulses enter a dispersive medium, they undergo significant broadening in time due to the spectral dependence of the group velocity, i.e. nonzero GVD. In absence of nonlinearities in the dispersive fiber, the temporal

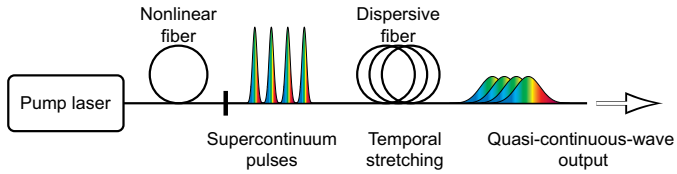

Figure 3.5. Schematic presentation of the concept of a simple fiber-based supercontinuum light source with the potential to emit quasi-continuous-wave radiation.

broadening process for a pulse with a given spectrum $P(\omega, 0)$ can be mathematically modeled using the simple expression for the complex spectral amplitude $A(\omega, z) = \sqrt{P(\omega, 0)}e^{i\beta(\omega)z}$, where $\beta(\omega)$ is the propagation constant of the fiber mode. Applying an inverse Fourier transform to the spectral amplitude allows to retrieve the corresponding pulse envelope $P(t, z) = \left|\mathcal{F}^{-1}\left\{A(\omega, z)\right\}\right|^2$ after the propagation distance z.

Note, that the initial phase information of the launched supercontinuum pulses can be neglected in the expression above, since the considered fiber lengths of the dispersive fiber yields a large GVD ($\beta_2 z$) [91].

Figure 3.6 shows the relative group delay ($\tau_g = L/v_g$) of the fundamental mode calculated for a long ($L = 100$ m) conventional single-mode fiber (SMF). Since the group delay is nonlinear with respect to the wavelength, different frequency components will experience different temporal delays. At the wavelengths in the vicinity of the ZDW (≈ 1280 nm), the group delay is nearly constant and therefore these components will propagate over a long distance with negligible separation in time. Hence, efficient temporal broadening of a supercontinuum pulse will not only depend on the spectral width but also on the spectral range. According to the calculations presented in Publication I, conventional telecommunication SMFs provide sufficient temporal broadening in the visible spectral range already at moderate lengths (~ 100 m).

Apart from the length, the selection of the dispersive fiber also has to ensure

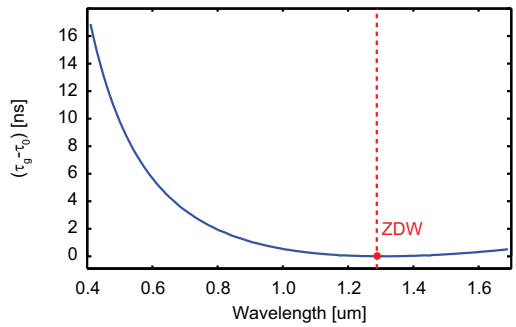

Figure 3.6. Group delay for a 100 meter long conventional SMF. For convenience the group delay is shown relative to the group delay at ZDW.

that solitons cannot exist within the spectral range of the coupled supercontinuum. This becomes particularly important when high-power soliton-like features are contained in the launched supercontinuum pulse, as they might form solitons when propagating in the dispersive fiber.

Alternatively, supercontinuum pulses can also be temporally broadened by means of intermodal dispersion in multimode fiber. In this case, the intermodal dispersion is usually stronger than chromatic dispersion and modeling of the temporal broadening can be based on the time response function of the fiber. The large spectral width of the supercontinuum, however, requires also to take chromatic dispersion into account, as described in Publication I.

The choice of dispersive fiber, either single-mode or multimode, will affect the spatial properties of the output light wave. A single-mode fiber naturally provides high spatial coherence of the output beam while the use of multimode fiber simplifies input light coupling and allows for the transmission of higher powers. It must be noted that if a multimode fiber is used as the dispersive fiber, any spatial filtering of the output light will effectively reduce the contribution of intermodal dispersion.

At some point, given a sufficiently long fiber, the propagating pulses will be stretched beyond the pulse-to-pulse period and start to overlap. As a result, the output power smoothes and becomes nearly constant (P_{avg}) with superimposed remaining variations (δP), as shown in Fig. 3.7. These fast fluctuations result from the temporal envelope of the stretched supercontinuum pulses and would ideally vanish for smooth envelopes. For pulses stretched by chromatic dispersion only, the spectrum of the input supercontinuum pulse determines the temporal envelope of the stretched pulse [91–93] and thus the temporal fluctuations at the output. In Publication I, we demonstrated that the fast variations can be minimized by proper selection of pulse repetition rate and fiber length.

In general, the noise characteristics of a light source can be quantified in terms of relative intensity noise (RIN). In practice, only the noise power within the range of frequencies determined by the limited response time of the optical detector is of interest. Therefore, noise characteristics of a light source are typically presented in terms of RIN power spectral density (PSD). Figure 3.8 shows the calculated RIN PSD for the example in Fig. 3.7, neglecting any other noise contributions apart from the residual intensity variations due to the pulse overlap. The root-mean-square RIN for a detector with a bandwidth of 350 MHz has been calculated as function of the pulse repetition rate and the fiber length in Publication I. These calculations show that a noise-to-

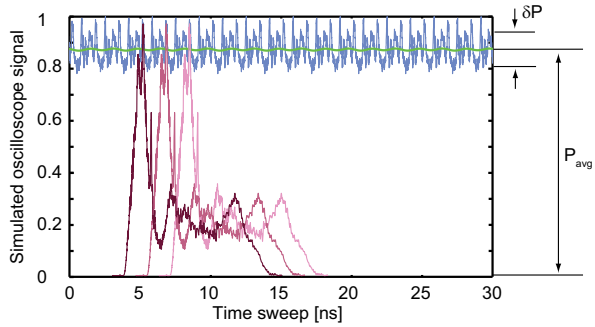

Figure 3.7. Temporal overlap of stretched supercontinuum pulses is illustrated exemplarily for 3 pulses emitted at repetition rate of 1 GHz. Also shown, the time dependence of the total power (blue) together with the signal expected for a detector with a 350 MHz bandwidth response (green).

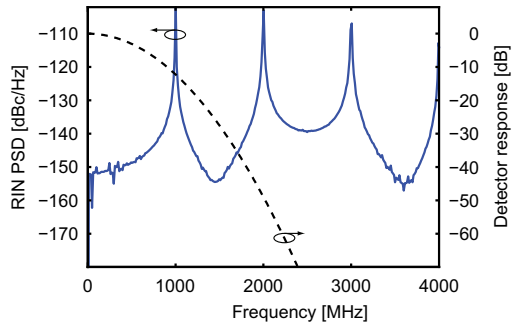

Figure 3.8. Power spectral density of relative intensity noise (solid line) calculated for the light intensity after 100 m of conventional telecommunication SMF and for an input pulse repetition rate of 1 GHz. The electrical response of a detector with a bandwidth of 350 MHz is also shown (dashed line). [Publication I]

mean power ratio lower than 1 % can already be achieved with moderate fiber lengths and pulse repetition rates.

The concept of the light source presented in Publication I thus allows for the generation of broadband continuous-wave light with a tailored spectrum at low noise levels. These properties are beneficial for many applications in high resolution imaging and spectroscopy.

3.3 Supercontinuum in multimode fibers

The high nonlinearity of MOFs originates from the strong field confinement achieved when these fibers are designed with a small core and a high core-cladding index contrast. Although typically only the fundamental mode is effectively excited, these MOFs can in principle support numerous transverse spatial modes [42, 63].

Earlier experiments have pointed out the importance of intermodal nonlin-

ear effects and demonstrated that a supercontinuum may also be generated in higher-order modes (HOMs) [94–96]. The complexity of SCG itself and the influence of intermodal phenomena in particular have mostly limited the theoretical studies of the pulse propagation in multimode MOFs to simple cases only [83, 85, 97–99].

Only recently, the theoretical framework has been successfully extended to enable the study of pulse propagation in multimode fibers taking into account an, in principle, unlimited number of modes [18, 19]. The derived multimode generalized nonlinear Schrödinger equation (MM-GNLSE) comprises apart from the common nonlinearities, wavelength dependent nonlinear mode couplings and was first applied to study the dynamics of intermodal nonlinear effects in femtosecond SCG. With this extended theoretical framework, a number of interesting applications have opened up. For instance, one can make use of the distinct dispersion characteristics of the HOMs for deep-ultraviolet SCG [16, 96]. The anomalous dispersion regime of the HOMs is shifted to wavelengths shorter than what can be achieved with the fundamental mode, so that efficient spectral broadening on the blue side of the pump wavelength can be realized [17, 100–102]. Other recent applications of the MM-GNLSE include the modeling of space division multiplexing [103, 104] and the high-average-power SCG in optical fibers [105].

In the original work of Poletti and Horak, the MM-GNLSE was solved numerically using the split-step Fourier method (SSFM) [19]. This method is widely used for solving the generalized nonlinear Schrödinger equation (GNLSE) due to its simplicity in programming and the relatively low computational complexity. However, the simplicity comes at the price that the simulations must be performed multiple times with different step sizes in order to estimate the error. Several improvements were proposed to the SSFM, such as a variable step size defined as a function of propagation distance or an adaptive step size derived from a local error estimate [106, 107]. This makes programming of the solver more complex and requires very thorough optimization, as otherwise the gain in computation speed may be lost. In particular, this holds for multimode simulations where the computational complexity rapidly increases with the number of modes [19].

Direct solving of the GNLSE is possible in the frequency domain where the equation can be formulated and solved as a system of ordinary differential equations (ODEs) [14, 108]. Despite a higher computational demand, compared to SSFM, the benefit of this approach is that many general purpose ODE solvers are readily available and they are highly optimized and efficient.

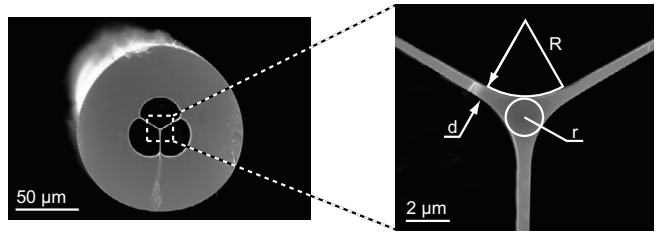

Figure 3.9. SEM image of the suspended-core fiber with the inset showing the close-up view of the core region.

Providing much easier implementation, many existing ODE solvers also contain error control and adaptive step-size integration algorithms which allow for faster convergence of the solution. Following this path, we have demonstrated in Publication II how the MM-GNLSE can be reformulated in the frequency domain into a system of ODEs, resulting in the development of an alternative numerical solver. As an example, the developed solver was used to demonstrate the polarization dynamics of SCG in two degenerate modes of a non-birefringent MOF.

In Publication III we used the MM-GNLSE solver for modeling the SCG in a three-hole silica suspended-core fiber (SCF), see also [109], and studied the influence of HOMs both experimentally and numerically.

A scanning electron microscopy (SEM) image of the SCF end facet is shown in Fig. 3.9. Before taking this image, the end facet and the outer surface of the fiber tip were coated first with 1.5 nm of titanium and then with a 20 nm thick gold layer. The metal layer prevents the charge build-up by allowing the current flow to the specimen holder and therefore significantly improves the image quality. The coating of the end facet was performed at a normal deposition angle, avoiding possible distortions of the fiber geometry due to metal addition.

We find that in the vicinity of the core the fiber geometry can be described by three parameters: the strand thickness near the core ($d \approx 600$ nm), the in-circle radius of the core ($r \approx 875$ nm) and the radius of curvature of the air hole near the core ($R \approx 3350$ nm), as shown in Fig. 3.9.

The waveguiding properties of the SCF were obtained using FEM mode-analysis applied to the geometry of the fiber's cross-section. For this analysis, the accurate geometry was obtained by first converting the SEM image into vector format and then properly scaling it to the fiber dimensions. We have found that the fiber core can support up to 12 modes in the vicinity of 780 nm, which is the operating range of the tunable mode-locked Ti:sapphire laser used in the experiments. The wavelength dependence of the GVD parameters and

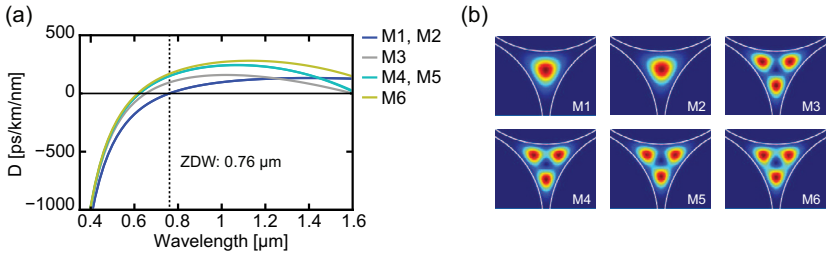

Figure 3.10. GVD parameters (a) and mode-intensity profiles (b) of the six lowest-order modes in the SCF obtained using FEM mode-analysis.

mode-intensity profiles for the six lowest order modes are shown in Fig. 3.10. For this fiber, the wavelength of zero-dispersion in the fundamental mode is located at 760 nm while the ZDWs of HOMs are located around 600 nm. We found that modes M1 and M2 as well as M4 and M5 form degenerate pairs which differ only in their polarization properties.

Nonlinear spectral broadening in the SCF was studied by pumping the fiber with 150 fs long light pulses emitted by a wavelength tunable mode-locked laser operating at a repetition rate of 82 MHz. Optimized for the highest transmission, the light pulses were coupled with a microscope objective into the fiber core. The coupling efficiency was estimated by measuring the average power at the fiber output and in front of the objective. The spectra of the supercontinuum generated in the fiber were recorded with an optical spectrum analyzer for several pump wavelengths and pulse powers. Additionally, the light emitted from the fiber was imaged through interchangeable bandpass filters onto a charge-coupled device (CCD) camera for recording the near-field images. Figure 3.11 shows the spectrum and the set of near-field images recorded for pump pulses at 780 nm with a peak power of 10.6 kW. Additional spectra measured under different pump conditions are presented in Publication III.

The near-field images, shown in Fig. 3.11, provide clear evidence that in addition to the fundamental mode the HOMs are also excited in the fiber. Over most of the spectral range, the near-field images resemble intensity profiles similar to the one expected from the fundamental mode and only in the vicinity of the pump wavelength the HOMs become apparent.

In principle, there are two possible origins for the presence of spectrally broadened light in the HOMs. The first possibility is that the light is initially coupled only into the fundamental mode and is later transferred to HOMs via nonlinear interactions. Alternatively, the HOMs can be initially excited with sufficient power for independent spectral broadening. In order to study

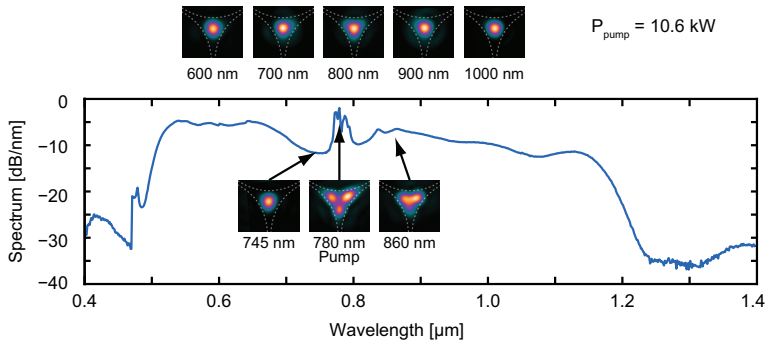

Figure 3.11. Measured spectrum of the supercontinuum generated in the SCF by pump pulses with a wavelength of 780 nm and a peak power of 10.6 kW. Also shown, the near-field images recorded at the fiber output for selected wavelengths.

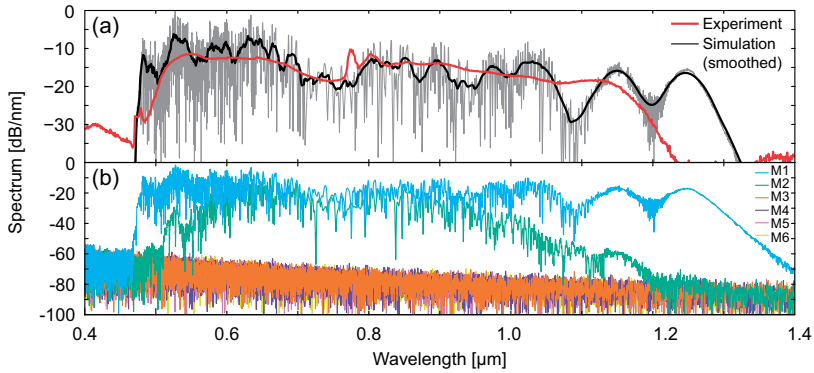

Figure 3.12. Simulated spectrum (gray line and black line (smoothed)) shown in (a) together with the measured spectrum (red line) is obtained from the coherent sum of the modal contributions presented in (b). The simulation was performed for a single pump pulse coupled entirely into mode M1. [Publication III]

further the origin and role of the HOMs in the spectral broadening, we perform a detailed multimode numerical analysis utilizing the solver described in Publication II.

First, the simulations are performed assuming that the full pump power is coupled only into mode M1. However, all modes require the inclusion of noise as otherwise no interaction between the modes is possible. In Fig. 3.12(a), the simulated spectrum for a single pump pulse is compared with the measured one for the same pump conditions. We see that the simulated spectrum is much broader than the measurement. Furthermore, no power transfer to HOMs is observed except to the degenerate mode M2, see Fig. 3.12(b).

The significant differences in the modal dispersion profiles yield a short modal walk-off length between the non-degenerate modes and thus reduce the interaction efficiency. In addition, the magnitude of coupling coefficients

$Q^{(1,2)}_{plmn}$ (as defined in Publication II) are also an important indicator for the efficiency of intermodal interactions. For the present fiber geometry, only those $Q^{(1,2)}_{plmn}$ coefficients, which are attributed to intramodal nonlinearities and intermodal XPM, have the largest magnitude. Within the degenerate mode pair (M1 and M2), the well satisfied phase-matching condition, will also enable energy transfer by intermodal FWM. This effect is, in fact, responsible for the appearance of the broad spectrum observed in mode M2. From this study, we conclude that intermodal interaction is in general strongly suppressed so that the experimentally observed HOMs must have been excited initially.

Ideally, the power coupled into each fiber mode can be found from decomposition of the input field in terms of mode fields. We calculated the coupling efficiency by integrating the overlap of the incident field with the mode fields [110]. Approximating the laser beam with an ideal Gaussian beam with waist radius of 648 nm and aligning it perfectly with the core, we find that almost all pump power is coupled to the degenerate fundamental mode, with the power ratio between M1 and M2 depending on the beam polarization. Any lateral offset of the beam results in more efficient excitation of the HOMs with relative power fractions strongly depending on both the offset direction and the beam polarization. Calculating the total coupling efficiency at a grid of pump beam offsets, we obtain the coupling maps, shown in Fig. 3.13(a) for three polarization angles arbitrarily selected along each of the strands. The coupling maps clearly indicate that the maximal coupling persistently occurs at an offset location with only slight dependence on the beam polarization.

For the offset point with maximal coupling we identify at a polarization angle ($\phi = 90^o$) the relative modal power fractions as summarized in Tab. 3.1. Only approximately 57 % of the full pump power (10.6 kW) is coupled into the fundamental mode at this beam alignment while the remaining pump power is distributed among the HOMs. Using these modal fractions for initial mode excitation we repeated the simulation and the resulting spectrum together with individual mode contributions is presented in Fig. 3.14. Under these conditions, the total spectrum is in a good agreement with the experiment. The spectrum in the fundamental mode reproduces the spectral width of the measured spectrum, see Fig. 3.14(b), while the overall broadening of the HOMs

M1	M2	M3	M4	M5	M6
48.8	8.7	5.4	21.1	0.0	16.0

Table 3.1. Fractional mode power at the pump beam polarization aligned along vertical strand of the fiber ($\phi = 90^o$).

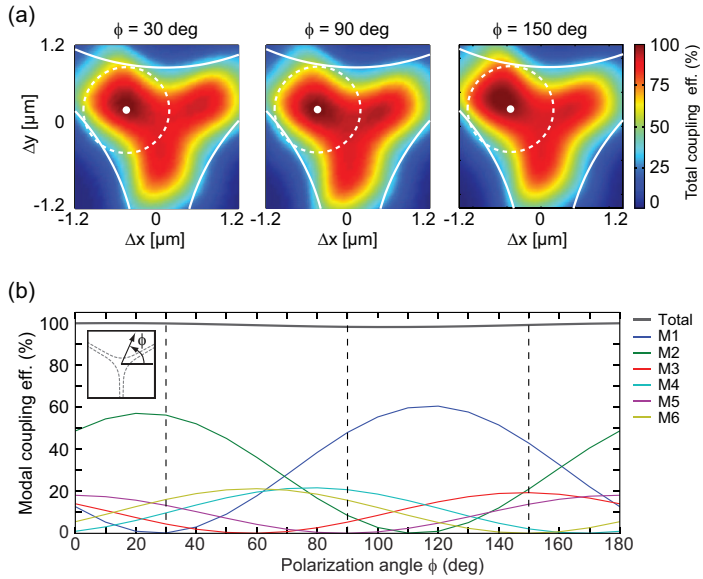

Figure 3.13. (a) Coupling efficiency maps calculated for an ideal Gaussian beam with waist radius of 648 nm and three polarization angles. (b) Coupling efficiencies for each mode depending on beam polarization plotted at the offset of maximal coupling to the fiber core. [Publication III]

is only about 200 nm, see Fig. 3.14(c). The spectral broadening in the HOMs is dominated by soliton fission process while low initial power and significant separation from the ZDWs of these modes prevent the generation of dispersive waves. Furthermore, the simulated HOM spectra cover a wavelength range similar to what has been observed by the near-field images, shown in Fig. 3.11.

The results presented in Publication III demonstrate that depending on the pump beam size relative to the fiber geometry, the alignment with maximal coupling to the fiber does not necessarily mean that only the fundamental mode is excited. For some specific fiber geometries like the suspended-core fiber the maximal coupling to the fiber may be found at offset locations which also results in more efficient excitation of the HOMs.

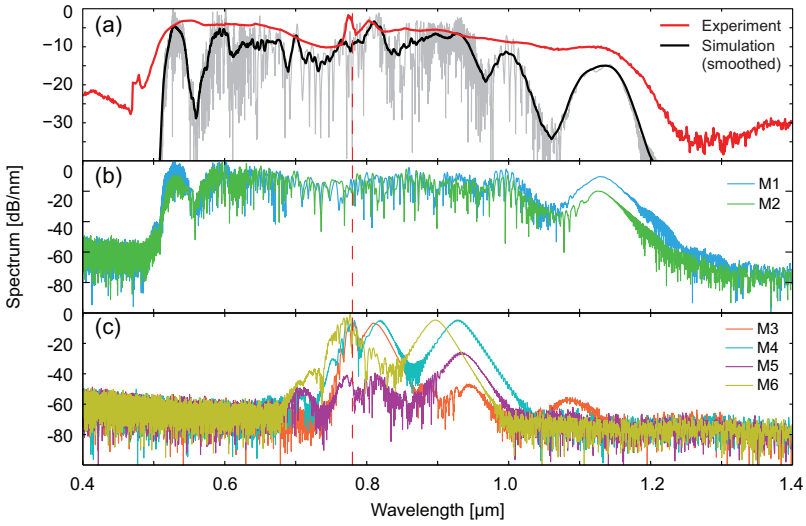

Figure 3.14. Simulation results assuming non-zero initial excitation of HOMs with power distribution as given in Tab. 3.1. In (a) the simulated supercontinuum (gray line and black line (smoothed)) is compared to the measured spectrum (red line). The modal spectral contributions are presented separately in (b) and (c). [Publication III]

4. High-resolution optical interferometry

In the most general way, interferometry can be described as a measurement technique that utilizes the superposition of waves to obtain the information about the measuring object. While interferometry can be applied to waves of different nature, this chapter, however, focuses only on the interference between optical waves.

After introducing the basics of interferometry, two high-resolution interferometric setups are described: A stroboscopic white-light interferometer for the study of out-of-plane vibration fields in a micro-mechanical resonator and a simple fiber-based interferometer for the measurement of the complex refractive index of gaseous analytes.

4.1 Basics of interferometry

When a monochromatic plane wave of initial amplitude A_0 propagates through a homogenous and isotropic medium, the amplitude at propagation distance z and time t can be described by

$$A(z,t) = A_0 \cdot e^{ik_0 nz} \cdot e^{-i\omega t}, \tag{4.1}$$

where $k_0 = \omega/c_0$ is the free-space wavenumber, c_0 is the speed of light, n is the refractive index of the medium and ω is the angular frequency. Consequently, at a fixed moment in time, the phase of the propagating wave depends on both the refractive index and the propagation distance. Thus, the optical properties of the medium can, in principle, be retrieved from an analysis of the wave. However, the high optical frequencies ω make it impossible to measure the wave amplitude directly, as conventional optical detectors are limited to the measurement of the time averaged intensity $I(z) = \left\langle |A(z,t)|^2 \right\rangle_t$ only; here $\langle\rangle_t$ denotes the time average over multiple optical cycles. An alternative solution to determine the optical properties of the medium is to compare the wave after propagation through the medium with a reference wave. This is the

main principle behind interferometric techniques. In optics, usually both the probe and reference waves are generated by dividing an incoming wave into two parts. After the propagation through the sample and reference paths, respectively, both waves are combined, and the resulting total intensity can be measured. The total intensity observed on the detector I_{det} is related to the superposition of the wave amplitudes and can be expressed as

$$I_{det} = \left\langle |A_p(z_p,t) + A_r(z_r,t)|^2 \right\rangle_t = I_p + I_r + 2\sqrt{I_p I_r} cos(\Delta\phi), \tag{4.2}$$

where A_p, A_r and I_p, I_r are the amplitudes and the intensities of the probe and reference waves, respectively. Furthermore, the total intensity I_{det} strongly depends on the phase difference $\Delta\phi$ between the two waves at the detector. Combining Eqs. 4.1 and 4.2, the phase difference can be related to the refractive indices (n_p, n_r) and the geometric path lengths (z_p, z_r) of the respective propagation paths according to

$$\Delta\phi = k_0 \left(n_p z_p - n_r z_r\right). \tag{4.3}$$

In Eq. 4.3 the quantity $(n_p z_p - n_r z_r)$ is often referred to as the optical path length difference (OPLD). Thus, interferometric techniques allow not only the measurement of the refractive index of a medium but also the measurement of distances.

Michelson and Mach-Zehnder interferometers. The devices that make use of interference between waves are called interferometers. Figure 4.1 illustrates two common interferometer setups, a Michelson and a Mach-Zehnder interferometer. In a Michelson interferometer, shown in Fig. 4.1(a), the beam from the light source S is divided by a beam-splitter (BS) into a reference and a probe beam. After reflection from the mirrors at the ends of the corresponding interferometer arms, the beams are recombined by the same beam-splitter. The total intensity of the superposed waves can then be detected at the output, as shown in Fig. 4.1(a). In case when the refractive indices in both interferometer arms are equal ($n_s = n_r = n$), any displacement Δz of the mirror M2 along the beam path will directly influence the phase difference according to $\Delta\phi = k_0 n \cdot 2\Delta z$. Consequently, changes in the path length can be obtained directly from the measurement of intensity I_{det}, using Eq. 4.2.

The principle of refractive index measurement utilizing a Mach-Zehnder interferometer is illustrated in Fig. 4.1(b). In this setup, the beam from the light source S is divided by the first beam splitter (BS1) into two beams. Guided along separate paths, the beams are combined by a second beam-splitter (BS2) and the intensity I_{det} can then be recorded at the output of the interferometer.

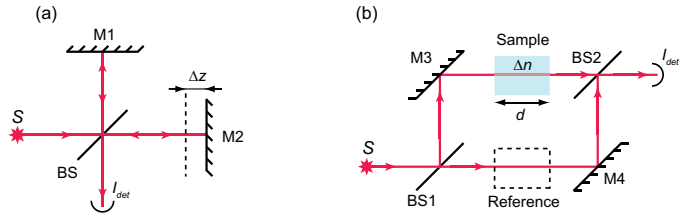

Figure 4.1. Illustration of a Michelson interferometer (a) and Mach-Zehnder interferometer (b) utilized for distance or refractive index measurements, respectively.

Note, that only one output is shown in Fig. 4.1(b) for clarity. When a sample with unknown refractive index is placed into one of the interferometer arms, the change of the refractive index causes a phase shift of $\Delta\phi = k_0 d \cdot \Delta n$, where d is the length of the sample, as shown in Fig. 4.1(b). Therefore, this setup is suitable to obtain the refractive index of the sample from the measurement of the light intensity at the detector.

4.2 White-light interferometry of vibrating microstructures

The sensitivity of interferometers to the OPLD has been utilized for high-resolution optical surface profilometry [111–116]. When replacing, for instance, one of the mirrors in a Michelson interferometer by a sample, an accurate height map of the sample can be obtained. However, from the measured phase difference an unambiguous determination of the surface height is only possible as long as changes in the path length remain within half of the wavelength, i.e. typically below a few hundred nanometers. While this is typically fulfilled in optical testing of smooth surfaces, like mirrors, samples with large step heights require a different approach for surface profilometry.

The ambiguity problem can be resolved by using a multiple-wavelength [117, 118] or low-coherence [119–122] light source for illumination. In case of low-coherence illumination, the superposed waves of each optical frequency contained in the broadband light combine to a localized interference pattern at the detector. Localizing this interference pattern, unambiguous mapping of the static surface topography becomes possible for step heights ranging from the nanometer to millimeter scale. This method is typically referred to as white-light interferometry (WLI) and is widely used for the characterization of miniaturized electromechanical components, such as microelectromechanical system (MEMS). It is also known as optical coherence tomography in biomedical applications [22, 69, 123].

In Publication IV, we describe a white-light interferometer and the data

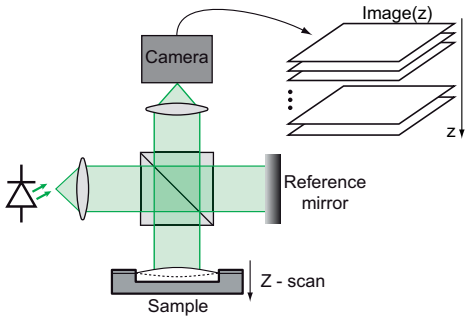

Figure 4.2. Experimental setup consisting of Michelson white-light interferometer. A collimated LED beam split into the sample and reference beams by a non-polarizing beam splitter. The returning beams are combined and imaged onto a camera equipped with a lens for microscopic imaging. During the measurement, the sample is translated in steps along the probe beam (Z-scan) at the same time recording the camera image for each step.

analysis method that allows for the mapping of out-of-plane surface vibration fields with sub-nm resolution and frequencies up to tens of MHz.

The experimental setup consists of a typical Michelson interferometer with the reference mirror in one arm and the sample in the second arm, as shown in Fig. 4.2. The sample is attached to a translator and can be precisely moved along the beam axis in order to scan the OPLD and record the interference fringe pattern for each surface point on the sample, as shown in Fig. 4.3(a) and Fig. 4.3(b). Then, by locating the white-light interferogram at each surface point, the relative height-map can be obtained for the entire surface.

Various methods have been developed to analyze white-light interferograms in order to obtain the height information. The simplest method is to locate the maximum of the interferogram under the assumption that it coincides with the zero-order fringe. This approach, however, is very sensitive to any intensity drift or noise. Alternatively, the calculation of the so-called "center of gravity" can also be used [124]. More precise methods extract the envelope of the interferogram and locate its center by a Gaussian fit, which requires that the employed light spectrum can be approximated by a Gaussian shape [125].

From the numerous analysis methods developed for WLI, the frequency domain analysis (FDA) approach described in [126, 127] was implemented. In this method, the interferograms at each pixel are first transformed into spatial-frequency domain. In the frequency domain, the spectral phase ϕ is a linear function of the wavenumber k with the slope unambiguously related to the location of the fringe pattern h and hence to the sample height ($\phi_{xy}(k) = h_{xy}k$). Since practical light sources are limited in the spectral width, the linearity of the phase can only be observed within a finite range of wavenumbers, as

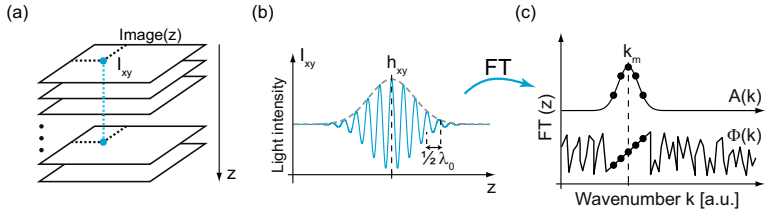

Figure 4.3. Schematic presentation of the frequency domain analysis (FDA) approach for processing WLI data. (a) During the measurement, a stack of images is acquired as a function of the varied OPLD (z-scan). When examining the light intensity data from a particular camera pixel through the stack, $I_{xy}(z)$, (b) a typical WLI interferogram with localized fringes is observed. (c) Applying a Fourier transform (FT) to the interferogram, the spectral amplitude content ($A(k)$) of this signal peaks at the wavenumber k_m, in the vicinity of which the spectral phase ($\Phi(k)$) is linear. [Publication IV]

shown in Fig. 4.3(c). An advantage of the FDA is that it does not require a specific spectral shape and can even tolerate possible spectral changes caused by the reflection from different materials.

Enhanced white-light interferometry. The resolution of WLI can be further improved by combining the fringe envelope localization measurement with detection of the interferometric phase.

The main idea behind this method is schematically illustrated in Fig. 4.4 for a step height sample. Locating the coherence envelope enables to unambiguously determine the sample height down to the fringe order. The analysis of the phase information can provide a high-resolution topography but suffers from the phase ambiguity. Combined, however, both approaches yield an unambiguous, high-resolution height-map, as shown on the right in Fig. 4.4. This improvement enables detection of sub-nanometer surface height features over a large dynamic range [121,126], and has made this method particularly attractive for MEMS.

In principle, for enhanced WLI the coherence envelope location and interferometric phase can be obtained with any of the available methods [125,127,128]. Here, we selected the FDA since it can simultaneously yield the envelope location and interferometric phase. While the envelope location is related to the slope of the spectral phase, as described earlier, the interferometric phase can be extracted from the spectral phase at the mean wavenumber k_m of the fringe pattern, see Fig. 4.3(c).

A detailed description of the FDA algorithm for the enhanced WLI is provided in the original publications of de Groot *et. al* [126,127,129].

Measurement of vibration fields. For capturing the instantaneous surface deformations of moving elements, the data acquisition in surface profiling is

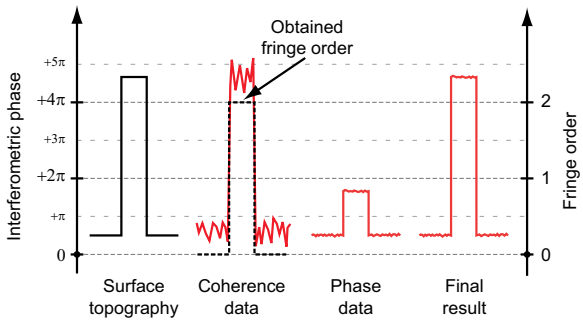

Figure 4.4. The basic principle of enhanced WLI is illustrated for a step-height sample. While the sample height can be obtained unambiguously with the coherence envelope localization, the interferometric phase information provides higher resolution data, however, with apparent ambiguity. The final result is then obtained by extracting the fringe order from the coherence data and using it to resolve the ambiguity in the phase data.

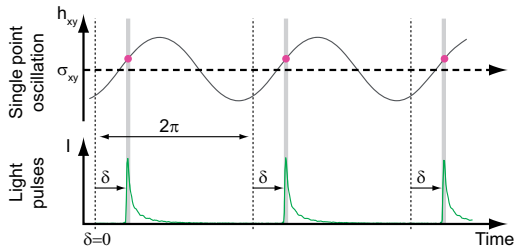

Figure 4.5. Stroboscopic measurement principle illustrated for a single point of an oscillating surface. The apparent motion of the point can be effectively "frozen" by illuminating it with short light pulses emitted at the oscillation frequency. By tuning the pulse delay δ the point location can be obtained at any oscillation phase.

typically too slow. In case of periodically vibrating surfaces, static surface profiling methods, such as WLI, can still be used when combined with stroboscopic illumination [116, 130–132]. In stroboscopic illumination, the light source emits pulses in synchronization with the sample excitation frequency, so that the sample is illuminated at the specific vibration phase only. This effectively "freezes" the periodic motion of the measured surface, as illustrated for a single surface point in Fig. 4.5. The instantaneous deformation at any vibration phase can then be measured by introducing a delay δ to the illuminating pulses with respect to the excitation signal. Provided the illumination pulse is short enough, this method allows for characterization of the dynamics of surface vibration at very high frequencies.

With stroboscopic illumination, WLI enables to obtain a set of instantaneous height maps, which cover the whole vibration period. These height maps can be either visualized directly or further analyzed to extract more detailed information on the vibration field. Although the instantaneous height-maps provide

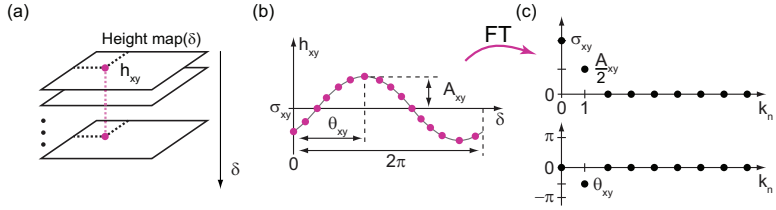

Figure 4.6. The surface vibration analysis was applied to a set of surface height maps (a) obtained over a complete vibration period. The surface deformation h_{xy} at a single spatial point as a function of δ is a sinusoid with a DC-offset σ_{xy} (b). Applying a Fourier transform, independently for each spatial point on the set of height maps, yields the sample surface topography (σ_{xy}) and both the absolute amplitude (A_{xy}) and phase (θ_{xy}) of the surface vibration (c). [Publication IV]

a good visualization of the vibrating surface and are thus often presented, they do not provide all the information available from the measurement. For instance, small parasitic effects on top of large-amplitude vibrations are difficult to identify from instantaneous deformation maps. Further vibration analysis is thus essential and of great interest for sample characterization.

For a harmonically oscillating surface, the height variation of a surface point can be described as

$$h_{xy}(\delta) = \sigma_{xy} + A_{xy}\cos(\theta_{xy} + \delta), \tag{4.4}$$

where σ_{xy} is the average height and A_{xy} and θ_{xy} are the amplitude and phase of the vibration. When analyzed for the entire surface, this yields the amplitude $A(x, y)$ and the phase $\theta(x, y)$ maps. These maps contain complete information on the surface deformation and can be used to calculate a 3D representation at an arbitrary vibration phase value.

We find the amplitude and the phase maps by measuring the surface deformation for a set of phase delays δ over the vibration period. Instead of directly fitting Eq. 4.4 into the height maps, we apply in Publication IV the computationally faster Fourier transform to the height variation at each point on the surface, as illustrated in Fig. 4.6. This method requires the instantaneous height maps to be measured at phase delays, which are evenly sampled over the complete vibration period such that $\delta \in [0; 2\pi)$. As a result, the first spectral bin of the discrete Fourier transform will contain the information on both, the amplitude and the phase of the vibration field, see Fig. 4.6(c). Additionally, the values at the zeroth spectral bin are related to the average surface topography $\sigma(x, y)$.

Figure 4.7 shows the measured amplitude and phase maps for a square-plate resonator [133, 134] vibrating at a frequency of 3.37 MHz. The very large dynamic range requires the amplitude map to be shown in logarithmic scale,

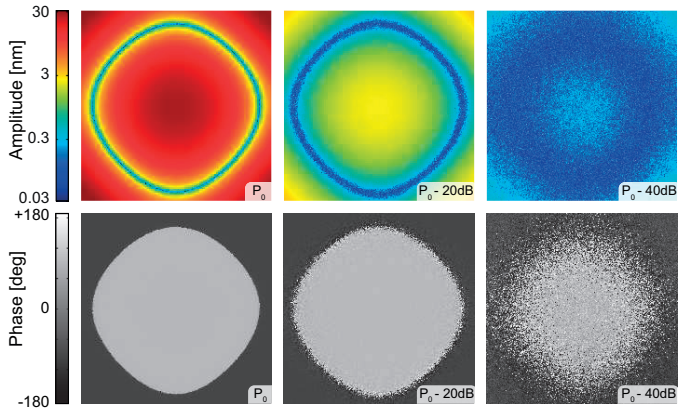

Figure 4.7. The set of measured vibration amplitude (first row) and phase (second row) data for the 3.37 MHz vibration mode. The vibration amplitude and phase data are also shown for three different input drive powers P_0, $P_0 - 20$ dB and $P_0 - 40$ dB. [Publication IV]

so that both strong and weak effects can be visualized simultaneously. At the nominal input drive power P_0, the amplitude data feature more than 40 dB of dynamic range, and the nodal line of the vibration mode is seen as a thin and deep minimum, with the corresponding phase data showing a sharp transition. In order to identify the minimum detectable amplitude, we reduced the excitation power levels. Decreasing the input drive power, and hence the vibration amplitude, serves to illustrate that the setup is capable of resolving vibration modes with a maximum amplitude of less than 300 pm. These results demonstrate that we can reach a minimum detectable vibration amplitude of less than 100 pm, which advances state-of-the-art stroboscopic white-light interferometry to the level comparable with full-field laser interferometry [135].

As is often observed, the maximum amplitude decreases with an increase in the vibration frequency. However, with the achieved amplitude detection limit, we are able to explore vibration fields at even higher frequencies. Figure 4.8 shows the amplitude and phase maps as well as the 3D views of instantaneous deformations for the vibration modes at frequencies of 7.18 MHz and 13.72 MHz.

Requirements on the light source. For the stroboscopic white-light interferometer described in Publication IV, the requirements on the light source can be divided into two categories, namely the spectral and temporal properties of the emitted light pulses.

Polychromatic illumination is the main requirement for WLI. A broader spectrum results in a more localized fringe pattern, and thus provides better resolution. However, the situation is different in case of enhanced WLI, where

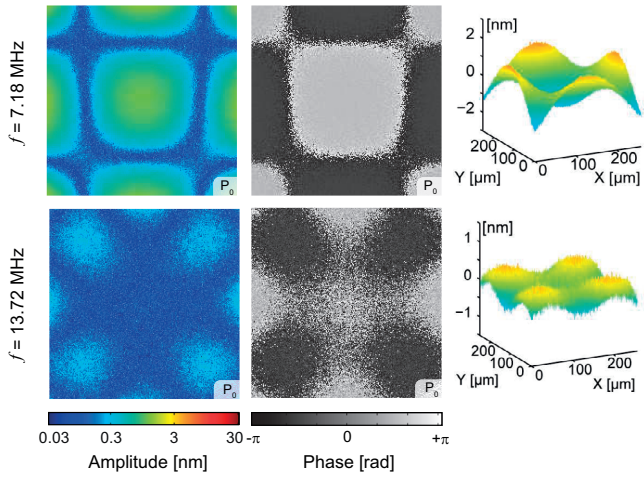

Figure 4.8. The set of measured amplitude (first column) and phase (second column) data for the 7.18 MHz and 13.72 MHz vibration modes. The amplitude and phase data can also be combined to create a 3D view of the instantaneous surface deformation at an arbitrary phase of the vibration (third column). The extremes of the colormaps for the 3D views correspond to the limits shown on each of the z-axes. [Publication IV]

the coherence and phase analysis give rise to opposite requirements on the light source spectrum.

While in enhanced WLI the coherence envelope is only utilized to extract the fringe-order, the resolution of the height determination depends entirely on the phase analysis. The narrower the light spectrum, the higher resolution can be obtained. Therefore, the optimal light spectrum has to be carefully selected. In Publication IV we have demonstrated that the bandwidth of 35 nm of a green light-emitting diode (LED) (central wavelength of 510 nm) was already close to optimal value, as it enabled resolution of vibration amplitudes below 100 picometers.

It is important to note that in practice, only the presence of noise limits the resolution obtainable from the analysis of fringe location. The theoretical resolution limit in WLI has been studied by Fleischer *et al.* [136]. The influence of both the noise level and the spectral properties of the light were analyzed in [136] based on signal theory. Therefore, their conclusions do not rely on the specific analysis method but rather describe the possible information capacity of the interferogram.

The duration of the illuminating pulse is an important factor in stroboscopic methods since it defines the temporal resolution. In general, the pulses must be much shorter than the typical time scale of the process being observed. For instance, in stroboscopic WLI, the finite pulse duration results in a decreased

visibility of the interference fringe pattern and an underestimated vibration amplitude [131]. Currently, LED-based light sources are widely used in WLI. However, their minimum pulse durations are limited to a few nanoseconds, which effectively enables stroboscopic illumination up to frequencies of a few tens of MHz. Shorter pulses can be obtained from laser-based light sources. Supercontinuum-based light sources are, in this respect, attractive candidates, as they provide the flexibility to tailor the spectral properties [9].

4.3 Simple interferometric gas refractometer

As was already pointed out in the first section of this chapter, the sensitivity of interferometers to the phase changes in a probe wave can also be employed for the precise measurement of the refractive index of various materials. This enables not only the characterization or detection of substances, but also allows for indirect analysis of the physical characteristics, such as pressure or temperature of the environment [56, 57]. In order to reach highest sensitivity, a good overlap of the probing light wave with the analyte is essential.

In this respect, the introduction of PCFs has been followed with the great interest. These fibers add, in addition to the numerous advantages that conventional optical fibers have brought to the sensing technology, the possibility for strong interaction of the guided light with the analyte infiltrated into the air holes [37, 47, 51, 137–139]. In particular, the class of HC-PBFs allows for a perfect overlap between the probing light beam and the analyte. The potential use of HC-PBFs as long sample cells, which require only smallest amounts of analyte to reach the highest sensitivity, has been recognized from the beginning and has inspired numerous detection schemes since then [46,48–50,52,140,141]. Although many of these devices promise high sensitivity and resolution, they are often limited to the measurement of either the real or imaginary part of the complex refractive index.

In Publication V, we show that spectrally resolved measurements of both the refractive index and absorption coefficient can be performed for a liquid or gaseous analyte using a simple, HC-PBF based interferometric setup. Furthermore, the proposed design is, in comparison to many other detection schemes, very simple but yet highly precise and does not require coating techniques with a nanometer precision, splicing or tapering of the fiber.

The experimental setup of the refractometer is based on a Mach-Zehnder-type interferometer with optical fibers placed into both the sample and the reference arms. A conventional SMF is used in the reference arm and an

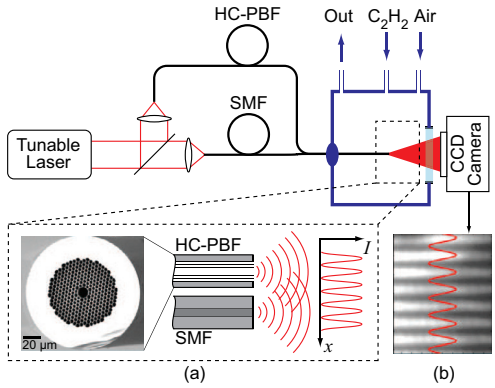

Figure 4.9. Schematic view of the gas refractometer setup. A close-up of the in parallel attached fiber outputs is shown in (a) together with a schematic illustration of the interference pattern formation. A SEM picture of the used HC-PBF is also presented. (b) Interference fringe pattern as recorded by CCD camera. [Publication V]

HC-PBF is utilized both as a gas cell and a waveguide in the sample arm, as shown in Fig. 4.9. Light from a wavelength tunable laser is focused after a beam-splitter cube into each fiber and guided along their lengths. The output fiber ends are placed parallel to each other so that the diverging output light overlaps and interferes on a CCD camera (see insets (a) and (b) in Fig. 4.9). In order to facilitate the filling of the core of the HC-PBF with gaseous analytes, the output fiber ends are placed in a sealed gas chamber with a window for the output light. The lengths of both fibers are chosen in order to balance the optical path lengths, however due to substantial differences in the dispersion of the fibers this can be achieved only within a narrow spectral range.

The measurement of the analyte's complex refractive index is based on the interference between optical waves. Variation of the refractive index in the sample arm results in a shift of the interference pattern observed on the CCD camera. By tracing this shift, we can precisely measure the change in refractive index. For example, this allows for recording of the spectral dependence of refractive index when the laser wavelength is scanned over the spectral range of interest, as was done in the present study. In addition, the spectrally dependent attenuation in the analyte defines the amplitude of the observed interference pattern. Therefore, both the refractive index and the absorption coefficient of an analyte can be measured simultaneously.

Analysis of the images acquired by the camera is performed numerically in the spatial frequency domain where the interference fringes give rise to the spectral amplitude A only at the specific frequency points, as shown in Fig. 4.10. At these frequency points the complex amplitude is related to

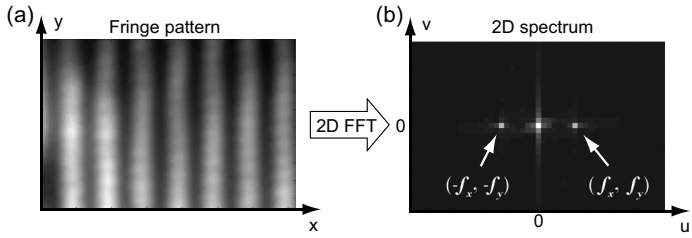

Figure 4.10. Recorded interference fringe pattern (a) and its two-dimensional spatial amplitude spectrum (b). The amplitude spectrum features the intense zeroth frequency component related to the average intensity and two side lobes which originate from the intensity modulation in the fringe pattern.

the fringe position and amplitude, which corresponds to the refractive index and the absorption coefficient, respectively. While the exact location of the frequency points (f_x, f_y) and $(-f_x, -f_y)$ is not important for the measurements, they must be clearly separated from the strong components near zero frequency. This can be achieved by increasing the number of fringes in the camera image, however, the noise and the discrete intensity measurement by the digital camera decrease the obtainable resolution when too many fringes become visible. In the present experiments the optimum resolution was found with seven fringes.

For monochromatic illumination it is nearly impossible to identify the zero-order fringe and thus the absolute value of the OPLD. Instead, a relative measurement technique was used. The measurement procedure consisted of two parts: First, the HC-PBF was infiltrated with the analyte and the fringe pattern was recorded while scanning the wavelength of the tunable laser over the spectral range of interest. Then, the same measurement was repeated for a reference medium of well known refractive index. While replacing the analyte with the reference medium, the fringe position was traced continuously in order to relate the two measurements. This technique, in addition, enabled for automatic accounting of the interferometer's intrinsic wavelength response. Compressed air was chosen as the reference medium since its refractive index can be precisely calculated [142–146].

The potential of the proposed refractometer was demonstrated by measuring both the absorption coefficient and the refractive index of an acetylene-air gas mixture within the spectral range from 1525 nm to 1545 nm, see Fig. 4.11. The results clearly resolve the resonant structure of the P branch of the $\nu_1+\nu_3$ band of acetylene gas.

Additionally, the measurement results were compared to a simple theoretical model based on the harmonic oscillator [147]. This model provides the

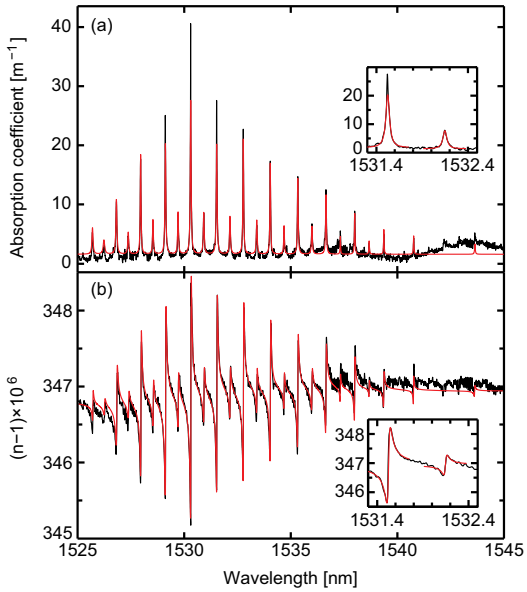

Figure 4.11. Measured absorption coefficient (a) and refractive index (b) for the air-acetylene gas mixture (black line). The smooth (red) curves represent a superposition of the results obtained by fitting each resonance independently as exemplarily shown for two resonances in the insets. [Publication V]

wavelength dependence of the refractive index and of the absorption coefficient in the vicinity of a single resonance. Thus, we first fitted each resonance independently, as shown in the insets of Fig. 4.11, and then added the fitted curves together for a comparison with the measurement, see red lines in main windows of Fig. 4.11. We find a good match between the theory and measurement.

The achieved resolution of $4 \cdot 10^{-7}$ RIU is mainly limited by the intermodal interference in the HC-PBF, which results in periodic variations of the fringe position and amplitude. This influence can be readily avoided by the use of a HC-PBF with suppressed HOMs [148,149], so that this concept has a potential for even higher resolutions.

5. Summary

Optical interferometry is widely applied in science and technology for investigating and measuring most diverse phenomena and properties, ranging from detection of small displacements, refractive index changes and surface roughness to astronomical observations. This thesis focuses on the development of bright, broadband light sources for interferometric applications, based on the generation of supercontinuum light in microstructured optical fibers (MOFs). Furthermore, two concrete examples of optical interferometry, the use of a stroboscopic white-light interferometer for vibration analysis of micro-mechanical resonators, and interferometric measurement of the refractive index of gases using a fiber-optic measurement setup are introduced, realized, and analyzed as potential applications for the broadband sources.

The first part of the thesis introduces a new concept for a broadband source, from which the light is emitted quasi-continuously in time, instead of the usual pulsed emission of supercontinuum sources. The main idea is based on dispersive temporal stretching of broadband light pulses beyond the pulse-to-pulse period to ideally reach constant output intensity. The light pulses, generated in a MOF, were coupled into a conventional optical fiber with either dominant chromatic or modal dispersion for temporal broadening. This concept was found to be able to provide intensity fluctuations below 1 % in the output light. Many applications in optical metrology, spectroscopy and imaging clearly benefit from such a bright continuous-wave light source.

A recent development in supercontinuum generation of light has been to extend the spectral coverage by using higher-order fiber modes for the nonlinear processes. In this thesis, a numerical solver for simulating such generation process was developed. The multimode generalized nonlinear Schrödinger equation was transformed, in the frequency domain, to a system of standard ordinary differential equations. This enabled the use of readily available ordinary differential equation solvers and thus gave a straightforward access to the

complex theoretical model. The potential of the approach was first verified in a simple case of non-birefringent multimode MOF pumped with femtosecond pulses, rendering a clear physical picture of the spectral broadening and the polarization dynamics of the generated output. The same approach was further applied to study the influence of higher-order modes on supercontinuum generation in a three-hole silica suspended-core fiber. The simulation results were compared to experimentally measured spectra, and a good agreement was found for the two. The detailed comparison shows that although the spectral broadening is mostly determined by the fundamental fiber mode, an excitation of the higher-order modes can considerably contribute to the spectral broadening, particularly in the vicinity of the pump wavelength.

The first example of optical interferometry performed in the thesis deals with a phase-shifting white-light interferometer that uses stroboscopic illumination. The setup was designed to characterize the dynamics of out-of-plane surface vibrations in electromechanical components. The performance of the interferometer was demonstrated by mapping surface vibration fields of a square-plate silicon MEMS resonator for a selection of out-of-plane vibration modes with resonance frequencies up to 14 MHz. A minimum detectable amplitude of less than 100 pm was achieved. This measurement technique enables characterization of small-amplitude vibrations at high frequencies and allows for the identification of weak parasitic effects on top of large-amplitude vibrations. In the present study, the highest measurable vibration frequency was limited by the duration of the light pulse obtained from a simple LED source. Switching to supercontinuum sources will allow much shorter pulses to be applied and, therefore, will open up new possibilities for the analyzes of much higher-frequency vibration fields. Moreover, a supercontinuum source provides flexibility in tailoring of the light spectral properties, which turns out to be an important factor in optimizing the resolution capabilities of the device.

As a second example of interferometric studies involving photonic crystal fibers, the thesis includes the development of a simple refractometer based on the use of a hollow-core photonic bandgap fiber as the sample container for gaseous analytes. The measurement geometry significantly reduces the amount of analyte required for the refractive index measurement while allowing at the same time a long interaction path. The refractive index is sensed through analyte-induced effective index variation in the hollow-core fiber. With this device, the refractive index of an air-acetylene mixture was measured with a resolution of $4 \cdot 10^{-7}$ RIU (refractive index units) in the spectral range from 1525 nm to 1545 nm.

Bibliography

[1] J. K. Ranka, R. S. Windeler, and A. J. Stentz, "Visible continuum generation in air-silica microstructure optical fibers with anomalous dispersion at 800 nm," Opt. Lett. **25**, 25 (2000).

[2] J. M. Dudley and G. Genty, "Supercontinuum light," Phys. Today **66**, 29 (2013).

[3] R. R. Alfano, *The Supercontinuum Laser Source: Fundamentals with Updated References* (Springer, New York, 2006), 2nd ed.

[4] T. W. Hänsch, "Nobel lecture: Passion for precision," (Nobelprize.org, Nobel Media AB 2013), http://www.nobelprize.org/nobel_prizes/physics/laureates/2005/hansch-lecture.html.

[5] J. L. Hall, "Nobel lecture: Defining and measuring optical frequencies: The optical clock opportunity and more," (Nobelprize.org, Nobel Media AB 2013), http://www.nobelprize.org/nobel_prizes/physics/laureates/2005/hall-lecture.html.

[6] S. T. Sanders, "Wavelength-agile fiber laser using group-velocity dispersion of pulsed super-continua and application to broadband absorption spectroscopy," Appl. Phys. B **75**, 799 (2002).

[7] J. Chou, Y. Han, and B. Jalali, "Time-wavelength spectroscopy for chemical sensing," IEEE Photon. Technol. Lett. **16**, 1140 (2004).

[8] K. Goda, K. K. Tsia, and B. Jalali, "Serial time-encoded amplified imaging for real-time observation of fast dynamic phenomena," Nature **458**, 1145 (2009).

[9] I. Kassamakov, K. Hanhijärvi, I. Abbadi, J. Aaltonen, H. Ludvigsen, and E. Hæggström, "Scanning white-light interferometry with a supercontinuum source," Opt. Lett. **34**, 1582 (2009).

[10] A. Mahjoubfar, K. Goda, A. Ayazi, A. Fard, S. H. Kim, and B. Jalali, "High-speed nanometer-resolved imaging vibrometer and velocimeter," Appl. Phys. Lett. **98**, 101107 (2011).

[11] P. Russell, "Photonic crystal fibers," Science **299**, 358 (2003).

[12] J. C. Knight, "Photonic crystal fibres," Nature **424**, 847 (2003).

[13] J. M. Dudley, G. Genty, and S. Coen, "Supercontinuum generation in photonic crystal fiber," Rev. Mod. Phys. **78**, 1135 (2006).

[14] J. M. Dudley and J. R. Taylor, *Supercontinuum Generation in Optical Fibers* (Cambridge University Press, New York, 2010).

[15] J. C. Travers, "Blue extension of optical fibre supercontinuum generation," J. Opt. **12**, 113001 (2010).

[16] A. Efimov, A. Taylor, F. Omenetto, J. Knight, W. Wadsworth, and P. Russell, "Nonlinear generation of very high-order UV modes in microstructured fibers," Opt. Express **11**, 910 (2003).

[17] Y. Chen, Z. Chen, W. J. Wadsworth, and T. A. Birks, "Nonlinear optics in the LP_{02} higher-order mode of a fiber," Opt. Express **21**, 17786 (2013).

[18] F. Poletti and P. Horak, "Description of ultrashort pulse propagation in multimode optical fibers," J. Opt. Soc. Am. B **25**, 1645 (2008).

[19] F. Poletti and P. Horak, "Dynamics of femtosecond supercontinuum generation in multimode fibers," Opt. Express **17**, 6134 (2009).

[20] D. J. Richardson, J. M. Fini, and L. E. Nelson, "Space-division multiplexing in optical fibres," Nat Photon **7**, 354–362 (2013).

[21] S. Mumtaz, R.-J. Essiambre, and G. P. Agrawal, "Nonlinear propagation in multimode and multicore fibers: Generalization of the manakov equations," J. Lightwave Technol. **31**, 398 (2013).

[22] D. Huang, E. A. Swanson, C. P. Lin, J. S. Schuman, W. G. Stinson, W. Chang, M. R. Hee, T. Flotte, K. Gregory, C. A. Puliafito, and J. G. Fujimoto, "Optical coherence tomography," Science **254**, 1178 (1991).

[23] P. Ryczkowski, A. Nolvi, I. Kassamakov, G. Genty, and E. Hæggström, "High-speed stroboscopic imaging with frequency-doubled supercontinuum," Opt. Lett. **38**, 658 (2013).

[24] K. Kao and G. Hockham, "Dielectric-fibre surface waveguides for optical frequencies," Proc. IEE **113**, 1151 (1966).

[25] T. Miya, Y. Terunuma, T. Hosaka, and T. Miyashita, "Ultimate low-loss single-mode fibre at 1.55 µm," Electron. Lett. **15**, 106 (1979).

[26] W. A. Gambling, "The rise and rise of optical fibers," IEEE J. Sel. Top. Quantum Electron. **6**, 1084 (2000).

[27] R. G. Huff and F. V. DiMarcello, "Hermetically coated optical fibers for adverse environments," Proc. SPIE **0867**, 40 (1988).

[28] K. E. Lu, G. S. Glaesemann, R. Vandewoestine, and G. Kar, "Recent developments in hermetically coated optical fiber," J. Lightwave Technol. **6**, 240 (1988).

[29] C. Kurkjian, J. T. Krause, and M. Matthewson, "Strength and fatigue of silica optical fibers," J. Lightwave Technol. **7**, 1360 (1989).

[30] J. C. Knight, T. A. Birks, P. Russell, and D. M. Atkin, "All-silica single-mode optical fiber with photonic crystal cladding," Opt. Lett. **21**, 1547 (1996).

[31] P. Russell, "Photonic-crystal fibers," J. Lightwave Technol. **24**, 4729 (2006).

[32] R. F. Cregan, B. J. Mangan, J. C. Knight, T. A. Birks, P. Russell, P. J. Roberts, and D. C. Allan, "Single-mode photonic band gap guidance of light in air," Science **285**, 1537 (1999).

[33] A. Bjarklev, A. S. Bjarklev, and J. Broeng, *Photonic Crystal Fibres* (Springer, USA, 2003).

[34] F. Zolla, G. Renversez, A. Nicolet, B. Kuhlmey, S. Guenneau, and D. Felbacq, *Foundations of Photonic Crystal Fibres* (Imperial College Press, Singapore, 2005).

[35] F. Benabid, "Hollow-core photonic bandgap fibre: New light guidance for new science and technology," Phil. Trans. R. Soc. A **364**, 3439 (2006).

[36] F. Poli, A. Cucinotta, and S. Selleri, *Photonic Crystal Fibers* (Springer, Dordrecht, 2007).

[37] O. Frazão, J. Santos, F. Araújo, and L. Ferreira, "Optical sensing with photonic crystal fibers," Laser & Photon. Rev. **2**, 449 (2008).

[38] Y. S. Skibina, V. V. Tuchin, V. I. Beloglazov, G. Shteinmaeer, I. L. Betge, R. Wedell, and N. Langhoff, "Photonic crystal fibres in biomedical investigations," Quantum Electron. **41**, 284 (2011).

[39] A. M. R. Pinto and M. Lopez-Amo, "Photonic crystal fibers for sensing applications," Journal of Sensors **2012**, 598178 (2012).

[40] T. A. Birks, J. C. Knight, and P. Russell, "Endlessly single-mode photonic crystal fiber," Opt. Lett. **22**, 961 (1997).

[41] J. Knight, T. Birks, R. F. Cregan, P. Russell, and J.-P. de Sandro, "Large mode area photonic crystal fibre," Electron. Lett. **34**, 1347 (1998).

[42] J. K. Ranka, R. S. Windeler, and A. J. Stentz, "Optical properties of high-delta air silica microstructure optical fibers," Opt. Lett. **25**, 796 (2000).

[43] R. Holzwarth, T. Udem, T. W. Hänsch, J. C. Knight, W. J. Wadsworth, and P. Russell, "Optical frequency synthesizer for precision spectroscopy," Phys. Rev. Lett. **85**, 2264 (2000).

[44] J. C. Knight, J. Broeng, T. A. Birks, and P. Russell, "Photonic band gap guidance in optical fibers," Science **282**, 1476 (1998).

[45] S. E. Barkou, J. Broeng, and A. Bjarklev, "Silica-air photonic crystal fiber design that permits waveguiding by a true photonic bandgap effect," Opt. Lett. **24**, 46 (1999).

[46] T. Ritari, J. Tuominen, J. C. Petersen, T. Sørensen, T. P. Hansen, H. R. Simonsen, and H. Ludvigsen, "Gas sensing using air-guiding photonic bandgap fibers," Opt. Express **12**, 4080 (2004).

[47] M. Skorobogatiy, "Microstructured and photonic bandgap fibers for applications in the resonant bio- and chemical sensors," Journal of Sensors **2009**, 524237 (2009).

[48] W. Jin, H. F. Xuan, and H. L. Ho, "Sensing with hollow-core photonic bandgap fibers," Meas. Sci. Technol. **21**, 094014 (2010).

[49] W. Yuan, G. E. Town, and O. Bang, "Refractive index sensing in an all-solid twin-core photonic bandgap fiber," IEEE Sensors J. **10**, 1192 (2010).

[50] M. Deng, C.-P. Tang, T. Zhu, Y.-J. Rao, L.-C. Xu, and M. Han, "Refractive index measurement using photonic crystal fiber-based Fabry-Perot interferometer," Appl. Opt. **49**, 1593 (2010).

[51] T. Ritari, J. Tuominen, J. C. Petersen, T. P. Hansen, and H. Ludvigsen, "Miniature wavelength references based on gas-filled photonic bandgap fibers," in "Proceedings of 30th European Conference on Optical Communication (ECOC '04)," (Stockholm, Sweden, 2004). p. Mo3.3.2.

[52] J. Tuominen, T. Ritari, J. Petersen, and H. Ludvigsen, "Gas filled photonic bandgap fibers as wavelength references," Opt. Commun. **255**, 272 (2005).

[53] Y. Hoo, W. Jin, H. Ho, J. Ju, and D. Wang, "Gas diffusion measurement using hollow-core photonic bandgap fiber," Sensor Actuat. B-Chem. **105**, 183 (2005).

[54] R. M. Wynne, B. Barabadi, K. J. Creedon, and A. Ortega, "Sub-minute response time of a hollow-core photonic bandgap fiber gas sensor," J. Lightwave Technol. **27**, 1590 (2009).

[55] Q. Shi, Z. Wang, L. Jin, Y. Li, H. Zhang, F. Lu, G. Kai, and X. Dong, "A hollow-core photonic crystal fiber cavity based multiplexed Fabry-Pérot interferometric strain sensor system," IEEE Photon. Technol. Lett. **20**, 1329 (2008).

[56] S. H. Aref, R. Amezcua-Correa, J. P. Carvalho, O. Frazão, P. Caldas, J. L. Santos, F. M. Araújo, H. Latifi, F. Farahi, L. A. Ferreira, and J. C. Knight, "Modal interferometer based on hollow-core photonic crystal fiber for strain and temperature measurement," Opt. Express **17**, 18669 (2009).

[57] Y. Geng, X. Li, X. Tan, Y. Deng, and Y. Yu, "Sensitivity-enhanced high-temperature sensing using all-solid photonic bandgap fiber modal interference," Appl. Opt. **50**, 468 (2011).

[58] A. W. Snyder and J. D. Love, *Optical Waveguide Theory* (Springer, Bristol, UK, 1983).

[59] E.-G. Neumann, *Single-Mode Fibers: Fundamentals*, no. v. 57 in Springer series in optical sciences (Springer, Berlin, 1988).

[60] J. C. Knight, T. A. Birks, P. Russell, and J. P. de Sandro, "Properties of photonic crystal fiber and the effective index model," J. Opt. Soc. Am. A **15**, 748 (1998).

[61] P. McIsaac, "Symmetry-induced modal characteristics of uniform waveguides - I: Summary of results," IEEE Trans. Microw. Theory Techn. **23**, 421 (1975).

[62] P. McIsaac, "Symmetry-induced modal characteristics of uniform waveguides - II: Theory," IEEE Trans. Microw. Theory Techn. **23**, 429 (1975).

[63] R. Guobin, W. Zhi, L. Shuqin, and J. Shuisheng, "Mode classification and degeneracy in photonic crystal fibers," Opt. Express **11**, 1310 (2003).

[64] D. Mogilevtsev, T. A. Birks, and P. Russell, "Group-velocity dispersion in photonic crystal fibers," Opt. Lett. **23**, 1662 (1998).

[65] A. M. Heidt, "Pulse preserving flat-top supercontinuum generation in all-normal dispersion photonic crystal fibers," J. Opt. Soc. Am. B **27**, 550 (2010).

[66] "COMSOL AB. [Online]. Available at http://www.comsol.com," .

[67] S. A. Diddams, D. J. Jones, J. Ye, S. T. Cundiff, J. L. Hall, J. K. Ranka, R. S. Windeler, R. Holzwarth, T. Udem, and T. W. Hänsch, "Direct link between microwave and optical frequencies with a 300 THz femtosecond laser comb," Phys. Rev. Lett. **84**, 5102 (2000).

[68] T. Ohara, H. Takara, T. Yamamoto, H. Masuda, T. Morioka, M. Abe, and H. Takahashi, "Over-1000-channel ultradense WDM transmission with supercontinuum multicarrier source," J. Lightwave Technol. **24**, 2311 (2006).

[69] I. Hartl, X. D. Li, C. Chudoba, R. K. Ghanta, T. H. Ko, J. G. Fujimoto, J. K. Ranka, and R. S. Windeler, "Ultrahigh-resolution optical coherence tomography using continuum generation in an air-silica microstructure optical fiber," Opt. Lett. **26**, 608 (2001).

[70] F. Shimizu, "Frequency broadening in liquids by a short light pulse," Phys. Rev. Lett. **19**, 1097 (1967).

[71] R. G. Brewer, "Frequency shifts in self-focused light," Phys. Rev. Lett. **19**, 8 (1967).

[72] R. R. Alfano and S. L. Shapiro, "Observation of self-phase modulation and small-scale filaments in crystals and glasses," Phys. Rev. Lett. **24**, 592 (1970).

[73] R. R. Alfano and S. L. Shapiro, "Emission in the region 4000 to 7000 Å via four-photon coupling in glass," Phys. Rev. Lett. **24**, 584 (1970).

[74] R. H. Stolen, E. P. Ippen, and A. R. Tynes, "Raman oscillation in glass optical waveguide," Appl. Phys. Lett. **20**, 62 (1972).

[75] E. P. Ippen and R. H. Stolen, "Stimulated Brillouin scattering in optical fibers," Appl. Phys. Lett. **21**, 539 (1972).

[76] R. H. Stolen and A. Ashkin, "Optical Kerr effect in glass waveguide," Appl. Phys. Lett. **22**, 294 (1973).

[77] E. P. Ippen, C. V. Shank, and T. K. Gustafson, "Self-phase modulation of picosecond pulses in optical fibers," Appl. Phys. Lett. **24**, 190 (1974).

[78] C. Lin and R. H. Stolen, "New nanosecond continuum for excited-state spectroscopy," Appl. Phys. Lett. **28**, 216 (1976).

[79] T. A. Birks, W. J. Wadsworth, and P. Russell, "Supercontinuum generation in tapered fibers," Opt. Lett. **25**, 1415 (2000).

[80] G. P. Agrawal, *Nonlinear Fiber Optics* (Academic Press, San Diego, 2001), 3rd ed.

[81] K. Washio, K. Inoue, and T. Tanigawa, "Efficient generation of near-I.R. stimulated light scattering in optical fibres pumped in low-dispersion region at 1.3 μm," Electron. Lett. **16**, 331 (1980).

[82] C. Lin, W. A. Reed, A. D. Pearson, and H.-T. Shang, "Phase matching in the minimum-chromatic-dispersion region of single-mode fibers for stimulated four-photon mixing," Opt. Lett. **6**, 493 (1981).

[83] S. Coen, A. H. L. Chau, R. Leonhardt, J. D. Harvey, J. C. Knight, W. J. Wadsworth, and P. Russell, "Supercontinuum generation by stimulated Raman scattering and parametric four-wave mixing in photonic crystal fibers," J. Opt. Soc. Am. B **19**, 753 (2002).

[84] N. I. Nikolov, T. Sørensen, O. Bang, and A. Bjarklev, "Improving efficiency of supercontinuum generation in photonic crystal fibers by direct degenerate four-wave mixing," J. Opt. Soc. Am. B **20**, 2329 (2003).

[85] D. A. Akimov, E. E. Serebryannikov, A. M. Zheltikov, M. Schmitt, R. Maksimenka, W. Kiefer, K. V. Dukel'skii, V. S. Shevandin, and Y. N. Kondrat'ev, "Efficient anti-Stokes generation through phase-matched four-wave mixing in higher-order modes of a microstructure fiber," Opt. Lett. **28**, 1948 (2003).

[86] R. H. Stolen, C. Lee, and R. K. Jain, "Development of the stimulated Raman spectrum in single-mode silica fibers," J. Opt. Soc. Am. B **1**, 652 (1984).

[87] G. Genty, M. Lehtonen, J. Broeng, M. Kaivola, and H. Ludvigsen, "Spectral broadening of femtosecond pulses into continuum radiation in microstructured fibers," Opt. Express **10**, 1083 (2002).

[88] A. V. Husakou and J. Herrmann, "Supercontinuum generation, four-wave mixing, and fission of higher-order solitons in photonic-crystal fibers," J. Opt. Soc. Am. B **19**, 2171 (2002).

[89] C. J. S. de Matos, S. V. Popov, and J. R. Taylor, "Temporal and noise characteristics of continuous-wave-pumped continuum generation in holey fibers around 1300 nm," Appl. Phys. Lett. **85**, 2706 (2004).

[90] J. C. Travers, A. B. Rulkov, B. A. Cumberland, S. V. Popov, and J. R. Taylor, "Visible supercontinuum generation in photonic crystal fibers with a 400W continuous wave fiber laser," Opt. Express **16**, 14435 (2008).

[91] K. Goda, D. R. Solli, K. K. Tsia, and B. Jalali, "Theory of amplified dispersive Fourier transformation," Phys. Rev. A **80**, 043821 (2009).

[92] T. Jannson, "Real-time Fourier transformation in dispersive optical fibers," Opt. Lett. **8**, 232 (1983).

[93] Y. Tong, L. Chan, and H. Tsang, "Fibre dispersion or pulse spectrum measurement using a sampling oscilloscope," Electron. Lett. **33**, 983 (1997).

[94] B. Crosignani and P. D. Porto, "Soliton propagation in multimode optical fibers," Opt. Lett. **6**, 329 (1981).

[95] Y. Vidne and M. Rosenbluh, "Spatial modes in a PCF fiber generated continuum," Opt. Express **13**, 9721 (2005).

[96] R. Cherif, M. Zghal, L. Tartara, and V. Degiorgio, "Supercontinuum generation by higher-order mode excitation in a photonic crystal fiber," Opt. Express **16**, 2147 (2008).

[97] M. Lehtonen, G. Genty, M. Kaivola, and H. Ludvigsen, "Supercontinuum generation in a highly birefringent microstructured fiber," Appl. Phys. Lett. **82**, 2197 (2003).

[98] Z. Zhu and T. G. Brown, "Polarization properties of supercontinuum spectra generated in birefringent photonic crystal fibers," J. Opt. Soc. Am. B **21**, 249 (2004).

[99] T. Chaipiboonwong, P. Horak, J. D. Mills, and W. S. Brocklesby, "Numerical study of nonlinear interactions in a multimode waveguide," Opt. Express **15**, 9040 (2007).

[100] J. Cheng, M. E. V. Pedersen, K. Charan, K. Wang, C. Xu, L. Grüner-Nielsen, and D. Jakobsen, "Intermodal Čerenkov radiation in a higher-order-mode fiber," Opt. Lett. **37**, 4410 (2012).

[101] B. Zwan, S. Legge, J. Holdsworth, and B. King, "Spatio-spectral analysis of supercontinuum generation in higher order electromagnetic modes of photonic crystal fiber," Opt. Express **21**, 834 (2013).

[102] T. J. Butcher, P. N. Anderson, R. T. Chapman, P. Horak, J. G. Frey, and W. S. Brocklesby, "Bright extreme-ultraviolet high-order-harmonic radiation from optimized pulse compression in short hollow waveguides," Phys. Rev. A **87**, 043822 (2013).

[103] G. Rademacher, S. Warm, and K. Petermann, "Influence of discrete mode coupling on the nonlinear interaction in mode-multiplexed systems," IEEE Photon. Technol. Lett. **25**, 1203 (2013).

[104] D. I. Kroushkov, G. Rademacher, and K. Petermann, "Cross mode modulation in multimode fibers," Opt. Lett. **38**, 1642 (2013).

[105] X.-h. Fang, M.-l. Hu, L.-l. Huang, L. Chai, N.-l. Dai, J.-y. Li, A. Y. Tashchilina, A. M. Zheltikov, and C.-y. Wang, "Multiwatt octave-spanning supercontinuum generation in multicore photonic-crystal fiber," Opt. Lett. **37**, 2292 (2012).

[106] A. Heidt, "Efficient adaptive step size method for the simulation of supercontinuum generation in optical fibers," J. Lightwave Technol. **27**, 3984 (2009).

[107] O. V. Sinkin, R. Holzlöhner, J. Zweck, and C. R. Menyuk, "Optimization of the split-step Fourier method in modeling optical-fiber communications systems," J. Lightwave Technol. **21**, 61 (2003).

[108] J. Hult, "A fourth-order Runge-Kutta in the interaction picture method for simulating supercontinuum generation in optical fibers," J. Lightwave Technol. **25**, 3770 (2007).

[109] I. Shavrin, P. Tvarožek, M. Koyš, K. Schuster, S. Novotny, and H. Ludvigsen, "Extremely white supercontinuum generation in three-hole suspended-core fiber," in "CLEO/Europe and EQEC 2011 Conference Digest," (Optical Society of America, 2011), p. CF_P16.

[110] M. Grabka, B. Wajnchold, S. Pustelny, and W. Gawlik, "Experimental and theoretical study of light propagation in suspended-core optical fiber," Acta Phys. Pol. A **118**, 1127 (2010).

[111] S. Petitgrand, R. Yahiaoui, K. Danaie, A. Bosseboeuf, and J. Gilles, "3D measurement of micromechanical devices vibration mode shapes with a stroboscopic interferometric microscope," Opt. Laser. Eng. **36**, 77 (2001).

[112] A. Bosseboeuf and S. Petitgrand, "Characterization of the static and dynamic behaviour of M(O)EMS by optical techniques: Status and trends," J. Micromech. Microeng. **13**, S23 (2003).

[113] Y. Emery, E. Cuche, F. Marquet, N. Aspert, P. Marquet, J. Kühn, T. Colomb, F. Montfort, F. Charrière, C. Depeursinge, P. Debergh, and R. Conde, "Digital holographic microscopy (DHM) for metrology and dynamic characterization of MEMS and MOEMS," Proc. SPIE **6186**, 61860N (2006).

[114] D. Malacara, *Optical Shop Testing* (John Wiley & Sons, Hoboken, N.J., 2007), 3rd ed.

[115] J. Schmit, J. Reed, E. Novak, and J. K. Gimzewski, "Performance advances in interferometric optical profilers for imaging and testing," J. Opt. A: Pure Appl. Opt. **10**, 064001 (2008).

[116] V. Heikkinen, K. Hanhijärvi, J. Aaltonen, K. Grigoras, I. Kassamakov, S. Franssila, and E. Haeggström, "Nondestructive static and dynamic MEMS characterization using supercontinuum scanning white light interferometry," Proc. SPIE **8250**, 825008 (2012).

[117] J. C. Wyant, "Testing aspherics using two-wavelength holography," Appl. Opt. **10**, 2113 (1971).

[118] Y.-Y. Cheng and J. C. Wyant, "Multiple-wavelength phase-shifting interferometry," Appl. Opt. **24**, 804 (1985).

[119] J. C. Wyant, "White light extended source shearing interferometer," Appl. Opt. **13**, 200 (1974).

[120] M. Davidson, K. Kaufman, I. Mazor, and F. Cohen, "An application of interference microscopy to integrated circuit inspection and metrology," Proc. SPIE **0775**, 233 (1987).

[121] P. Sandoz, R. Devillers, and A. Plata, "Unambiguous profilometry by fringe-order identification in white-light phase-shifting interferometry," J. Mod. Opt. **44**, 519 (1997).

[122] J. C. Wyant, "White light interferometry," Proc. SPIE **4737**, 98 (2002).

[123] P. H. Tomlins and R. K. Wang, "Theory, developments and applications of optical coherence tomography," J. Phys. D: Appl. Phys. **38**, 2519 (2005).

[124] R. Dändliker, E. Zimmermann, and G. Frosio, "Electronically scanned white-light interferometry: A novel noise-resistant signal processing," Opt. Lett. **17**, 679 (1992).

[125] K. G. Larkin, "Efficient nonlinear algorithm for envelope detection in white light interferometry," J. Opt. Soc. Am. A **13**, 832 (1996).

[126] P. de Groot and L. Deck, "Surface profiling by analysis of white-light interferograms in the spatial frequency domain," J. Mod. Opt. **42**, 389 (1995).

[127] P. de Groot, X. C. de Lega, J. Kramer, and M. Turzhitsky, "Determination of fringe order in white-light interference microscopy," Appl. Opt. **41**, 4571 (2002).

[128] A. Harasaki, J. Schmit, and J. C. Wyant, "Improved vertical-scanning interferometry," Appl. Opt. **39**, 2107 (2000).

[129] P. de Groot and L. Deck, "Three-dimensional imaging by sub-Nyquist sampling of white-light interferograms," Opt. Lett. **18**, 1462 (1993).

[130] A. Bosseboeuf, P. Nerin, P. Vabre, S. Petitgrand, and R. Yahiaoui, "Three-dimensional full-field dynamical characterization of micromechanical devices by stroboscopic white light scanning interferometry," Proc. SPIE **4400**, 36 (2001).

[131] P. de Groot, "Stroboscopic white-light interference microscopy," Appl. Opt. **45**, 5840 (2006).

[132] V. Heikkinen, I. Kassamakov, T. Paulin, A. Nolvi, and E. Hæggström, "Stroboscopic scanning white light interferometry at 2.7 MHz with 1.6 µm coherence length using a non-phosphor LED source," Opt. Express **21**, 5247 (2013).

[133] A. Jaakkola, P. Rosenberg, S. Asmala, A. Nurmela, T. Pensala, T. Riekkinen, J. Dekker, T. Mattila, A. Alastalo, O. Holmgren, and K. Kokkonen, "Piezoelectrically transduced single-crystal-silicon plate resonators," in "Proceedings of the IEEE Ultrasonics Symposium," (IEEE, New York, 2008, Beijing, China, 2008), p. 717.

[134] A. Jaakkola, J. Lamy, J. Dekker, T. Pensala, L. Lipiäinen, and K. Kokkonen, "Experimental study of the effects of size variations on piezoelectrically transduced MEMS resonators," in "Proceedings of the IEEE International Frequency Control Symposium," (Newport Beach, California, USA, 2010), p. 410.

[135] K. Telschow, V. Deason, D. Cottle, and J. I. Larson, "Full-field imaging of gigahertz film bulk acoustic resonator motion," IEEE Trans. Ultrason., Ferroelectr., Freq. Control **50**, 1279 (2003).

[136] M. Fleischer, R. Windecker, and H. J. Tiziani, "Theoretical limits of scanning white-light interferometry signal evaluation algorithms," Appl. Opt. **40**, 2815 (2001).

[137] J. Jensen, P. Hoiby, G. Emiliyanov, O. Bang, L. Pedersen, and A. Bjarklev, "Selective detection of antibodies in microstructured polymer optical fibers," Opt. Express **13**, 5883 (2005).

[138] L. Rindorf, J. B. Jensen, M. Dufva, L. H. Pedersen, P. E. Høiby, and O. Bang, "Photonic crystal fiber long-period gratings for biochemical sensing," Opt. Express **14**, 8224 (2006).

[139] L. Rindorf, P. E. Høiby, J. B. Jensen, L. H. Pedersen, O. Bang, and O. Geschke, "Towards biochips using microstructured optical fiber sensors," Anal. Bioanal. Chem. **385**, 1370 (2006).

[140] F. Benabid, F. Couny, J. C. Knight, T. A. Birks, and P. Russell, "Compact, stable and efficient all-fibre gas cells using hollow-core photonic crystal fibres," Nature **434**, 488 (2005).

[141] J. Sun and C. Chan, "Photonic bandgap fiber for refractive index measurement," Sensor. Actuat. B-Chem. **128**, 46 (2007).

[142] K. P. Birch and M. J. Downs, "An updated Edlén equation for the refractive index of air," Metrologia **30**, 155 (1993).

[143] K. P. Birch and M. J. Downs, "Correction to the updated Edlén equation for the refractive index of air," Metrologia **31**, 315 (1994).

[144] P. E. Ciddor, "Refractive index of air: New equations for the visible and near infrared," Appl. Opt. **35**, 1566 (1996).

[145] P. E. Ciddor and R. J. Hill, "Refractive index of air. 2. Group index," Appl. Opt. **38**, 1663 (1999).

[146] P. E. Ciddor, "Refractive index of air: 3. The roles of CO_2, H_2O, and refractivity virials," Appl. Opt. **41**, 2292 (2002).

[147] B. E. A. Saleh and M. C. Teich, *Fundamentals of Photonics* (John Wiley & Sons, Hoboken, N.J., 2007), 3rd ed.

[148] K. Saitoh, N. Florous, T. Murao, and M. Koshiba, "Design of photonic band gap fibers with suppressed higher-order modes: Towards the development of effectively single mode large hollow-core fiber platforms," Opt. Express **14**, 7342 (2006).

[149] M. N. Petrovich, F. Poletti, A. van Brakel, and D. J. Richardson, "Robustly single mode hollow core photonic bandgap fiber," Opt. Express **16**, 4337 (2008).

Aalto-DD 204/2013

ISBN 978-952-60-5472-8
ISBN 978-952-60-5473-5 (pdf)
ISSN-L 1799-4934
ISSN 1799-4934
ISSN 1799-4942 (pdf)

Aalto University
School of Electrical Engineering
Department of Micro- and Nanosciences
www.aalto.fi

BUSINESS +
ECONOMY

ART +
DESIGN +
ARCHITECTURE

SCIENCE +
TECHNOLOGY

CROSSOVER

DOCTORAL
DISSERTATIONS